

**Final Progress Report on PIDDP Grant NAG5-4548
Reflectron Time-of-Flight Mass Spectrometer (REMAS)
Instrumentation**

W.B. Brinckerhoff, R. W. McEntire*, and A. F. Cheng
The Johns Hopkins University Applied Physics Laboratory
11100 Johns Hopkins Rd
Laurel MD 20723-6099

* Principle Investigator
(240) 228-5410 phone
(240) 228-6670 fax

Contents

1. Overview

2. Progress

2.1 Sample Studies and Protocol Analysis

2.1.1 Energy Spectra and Abundance Analyses

2.1.2 Sample Type Variations

2.1.3 Elemental Analysis and Mineralogy

2.2 Instrumental Analysis

2.2.1 Reflectron Modeling

2.2.2 Grid Effects

2.2.3 Alignment

3. Future Directions

4. References

Appendix A. – Reprint

1. Overview

The restricted mass and power budgets of landed science missions present a challenge to obtaining detailed analyses of planetary bodies. *In situ* studies, whether alone or as reconnaissance for sample return, must rely on highly miniaturized and autonomous instrumentation. Such devices must still produce useful data sets from a minimum of measurements. The great desire to understand the surfaces and interiors of planets, moons, and small bodies had driven the development of small, robotic techniques with ever-increasing capabilities.

One of the most important goals on a surface mission is to study composition in many geological contexts. The mineralogical, molecular, elemental, and isotopic content of near-surface materials (regolith, rocks, soils, dust, etc.) at a variety of sites can complement broader imaging to describe the makeup and formative history of the body in question. Instruments that perform this site-to-site analysis must be highly transportable and work as a suite. For instance, a camera, microscope, spectrophotometer, and mass spectrometer can share several components and operate under a parallel command structure. Efficient use of multiple systems on a small rover has been demonstrated on the Mars Pathfinder mission.

The most capable instrument type for composition at the elemental and isotopic level is the ion mass spectrometer. A single peak is obtained for each isotope and detection limits and sensitivity can be excellent, even for miniature instruments. The ion mass spectrometer extracts and ionizes atoms and molecules from an analyte, which are separated and detected according to their mass-to-charge (m/z) ratios. (On bodies with significant atmospheres, the use of ions, rather than photons, requires sample acquisition and evacuation steps.) Several methods are available for sampling, including bombardment by atoms, ions, neutrons, or electrons, laser desorption/ablation, and thermal evaporation. For the direct analysis of unprepared solids, the laser has several advantages: it can both desorb and ionize, it can be small and low-power, it avoids target charging, and it can be used by other instruments in the suite. In addition, a pulsed laser provides the ideal "start pulse" when coupled with a time-of-flight (TOF) mass spectrometer. The TOF technique does not require magnets (which are heavy) or mass-scanning (which is data-intensive), making it very desirable for the types of surface missions described above [Meyer *et al.*, 1996].

The Laser Ablation Mass Spectrometer (LAMS), previously called the Reflectron Mass Spectrometer (REMAS) for this grant, under development in our laboratory, combines such a laser-TOF technique with a microscopic imager into a single instrument. As reported [Brinckerhoff *et al.*, 1998b; Brinckerhoff *et al.*, 2000], LAMS (Fig. 1) uses a miniature pulsed Nd:YAG laser to ablate and ionize a volume of approximately $2 \times 10^3 \mu\text{m}^3$ (1 ng at 2 g cm^{-3}). Ions are detected at times proportional to the square-root of their mass-to-charge ratios. Each laser pulse produces a full mass spectrum, typically 60 μs in duration for total elemental coverage.

There is no high-voltage source extraction in LAMS, meaning that ions are not accelerated away from the target surface to reduce their energy spread, unlike most TOF-MS instruments. This permits LAMS to be used in a totally contactless, or standoff, mode, minimizing the risk of

contamination. This mode is especially desirable on missions to airless bodies, such as asteroids and moons, because it does not require sample acquisition. The ion kinetic energy distribution is instead focused with a two-stage reflectron (Fig. 1). The reflectron temporally focuses ions of the same mass sufficiently to distinguish all elements and isotopes.

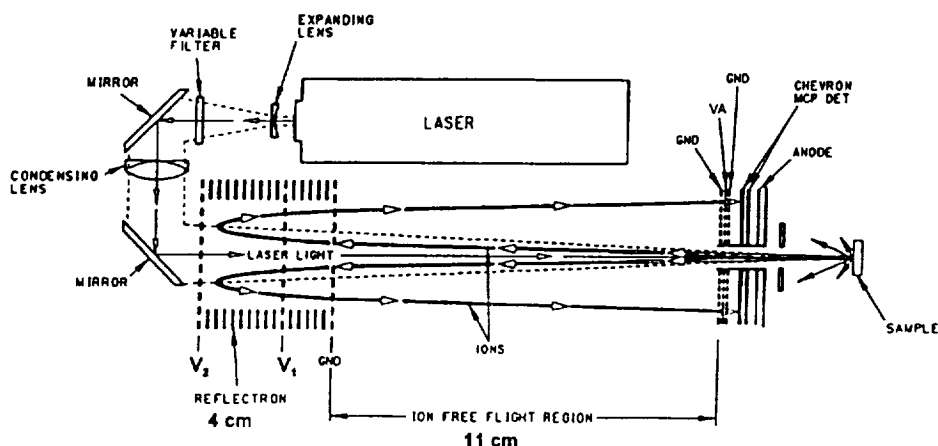


Figure 1 – Schematic of Laser Ablation Mass Spectrometer (LAMS).

The laser and micro-imager systems in LAMS share the main focus objective, and the instrument is coaxial with the optical path. That is, the laser passes through the back of the reflectron and hits the target at normal incidence. This design provides highly reproducible spectra, maximal imaging and laser spatial resolution, and a highly compact instrument. The imager is used to select a region of interest, and the laser then probes that region with 30-50 μm lateral and $\sim 0.1 \mu\text{m}$ depth resolution. Due to this geometry, a flight version of LAMS is potentially only 15-20 cm total length and ~ 2 kg total mass.

2. Progress

During the third year, we have made significant strides in the analysis and calibration of LAMS with multiple target materials. We have also reported on these advances in articles, abstracts, and oral presentations in the planetary science and mass spectrometry communities. The technical background of LAMS, and miniature laser TOF-MS in general, as well as some of the sample analyses conducted this year, have been summarized in an article [Brinckerhoff *et al.*, 2000] that has recently been published in *Review of Scientific Instruments*. The manuscript, entitled “Laser Time-of-Flight Mass Spectrometry for Space,” is included herein as Appendix A. This Progress Report will extend the results reported there and go into more detail on the specific protocols proposed for *in situ* measurements on planetary materials.

2.1 Sample Studies and Protocol Analysis

We have successfully analyzed a group of standard reference materials (SRM) from NIST, as well as several other terrestrial and meteorite samples, to determine the expected behavior of LAMS with unknown materials *in situ* on a landed mission. Detailed studies of NIST SRM

C1154a stainless steel, a tungsten carbide standard, and a terrestrial desert basalt are presented in the reprint (Appendix A). These analyses have given us a good sense of the levels of quantitative and qualitative information that can be obtained with a direct IR laser probe of unprepared targets. Essentially, we have learned that for most materials, both grain scale and bulk elemental abundances are statistically accessible to within 15%, and in several cases to within 10%, above a very low detection limit of approximately 10 - 20 ppm-atomic. By "statistically accessible" we mean that the number of laser shots needed to get good statistics is less than the number sufficient to ablate through a relevant mineralogical region. The spot size (30 - 50 μm diameter) and net crater depth (0.5 - 1 μm) are well within the observed range of spatial heterogeneity in the samples. This implies that complementary chemical and mineralogical information can be produced by LAMS. Grain-scale analysis can support mineral identification both from elemental abundances and from the simple presence or absence of key elements in a sequence of shots. Bulk abundances can support meteoritic classification through sequences or averaging of grain-scale analyses. In addition, all LAMS spectra give isotopic abundances that are accurate to within 5% on average. It is this *combined* capability (bulk semi-quantitative elemental and isotopic ratios, plus high-sensitivity qualitative microprobe analysis) that gives the LAMS technique its real power.

The progress in methods for analyzing various target materials is briefly reviewed in Sections 2.1.1 and 2.1.2. Initial results from a second meteorite sample and the relationship between elemental micro-analysis and first-order mineral identification are discussed in Section 2.1.3.

2.1.1 Energy Spectra and Abundance Analyses

LAMS operates in a windowed mode which produces high-resolution mass spectra with a two-stage reflectron [Brinckerhoff *et al.*, 1998b; Brinckerhoff *et al.*, 2000]. The window passes ions within a band of kinetic energies defined by the voltages (V_A, V_2), where V_A is the voltage on the analytical grid in front of the detector, and V_2 is the voltage on the grid at the rear of the reflectron (Fig. 1). While all ions with energies up to V_2 are repelled by the reflectron and are incident on the detector, only those with energies above $\sim 0.8 V_2$ are separated with sufficient resolution to analyze unit-mass isotopes ($R > 250$). Therefore, the analytical grid assembly serves to "reject" ions below this range.

By setting $V_A \approx 0.8 V_2$, only a fraction of the energy distribution is detected, introducing an instrumental abundance fractionation. Elements are ablated with a range of kinetic energies, and this distribution varies significantly between elements at ablation irradiances. A general trend we have studied is the increase of the mean energy with mass, for fixed irradiance. As such, a window of (80,100) V may capture only the upper-energy tail for carbon (C), while sampling the center of the iron (Fe) distribution. Several possible approaches to handle this fractionation have been studied, including (1) Determining relative sensitivity coefficients (RSC) for each element based on a single "standard" window; (2) Determining RSCs from a linear combination of a fixed set of windows; (3) Using a fixed ratio of $V_A:V_2$ and scanning the window from $V_2 = 200$ V to $V_2 = 33.6$ V in a sequence of nine windows, with several shots per window; (4) Using a set of medium-to-wide windows followed by several calibrated narrow windows; and (5) Focusing a broader range of energies in each shot with a higher-order reflectron.

For most target materials, approaches (3) and (4) have proved the most reliable with the current instrument design. Although approach (1) is the least demanding on resources (fewest laser shots and stored spectra, fixed voltages), and would be the least destructive analysis, reproducibility within one window has not been sufficient. The main reason for this is likely the variability of the kinetic energy distribution from shot to shot. The laser-target coupling can vary somewhat with surface makeup and morphology. In the range of GW cm^{-2} irradiances, the precise shape of the kinetic energy distribution can vary significantly with this coupling. With a fixed window, several elements will only be sampled in their tails (above or below their mean energies) which are most susceptible to this volatility. Approach (2) is a step in the right direction to capture the missing signals, but it still fails to equally sample elements with varying energy distribution widths, which have been observed for C, Co, and W in a standard carbide target [Brinckerhoff *et al.*, 2000]. By systematically scanning a wide energy range with a contiguous sequence of windows, and determining a standard deviation for each window, as in Approach (3), the fluctuations in energy distribution widths are averaged out and reproducible abundances are recovered. The trade-off in this method is that it required a large number of laser shots (> 100), and is thus essentially a bulk analysis. However, it is the least demanding of “standard curves” for RSCs and is thus appropriate for such analysis.

To obtain reproducible abundances with fewer laser shots (and less scanning) for some samples, we have also studied Approach (4). This approach works in materials that are somewhat more homogeneous than typical rocks – as may be the case in more primitive solar system materials. Wider windows ($V_A < 0.8 V_2$) capture a larger fraction of ions with each laser shot, at the expense of mass resolution. This cost can be tolerated if there are a few key elements/isotopes in every spectrum that are spaced more than 1 amu apart, ideally with no peaks between them. While the peaks from such elements are strongly tailed, their areas (and derived abundances) are reproducible. The data from a few wider-window laser shots may act as an *in situ* calibration for subsequent higher-resolution measurements. This approach has the significant advantage of using far fewer laser shots than Approach (3). The intrinsic limitation of this approach is the width of the window that can be used in the calibration step: for $V_A < V_I = 0.6 V_2$, some of the ions hitting the detector do not penetrate into the second stage of the reflectron, and are thus much more scattered in TOF.

Scanning of voltages can be largely avoided by employing a higher-order reflectron (Approach 5). We have modeled N-stage reflectrons, up to $N=6$, and have implemented one variation of the $N=5$ reflectron in hardware. Generally, introducing more stages into a reflectron should increase both the mass resolution and the energy range that is focused [Cotter, 1997]. Just as in the simplest $N=2$ case, optimal mass resolution is obtained for ions in the high-energy end of the distribution. That is, ions turned back in the second stage are focused as in a 2-stage reflectron, those turned back in the third stage as in a 3-stage reflectron, etc. To realize such a scheme in LAMS, the positions and voltages of the various stages must be chosen from a range of options, representing the family of focusing curves for a given N. We have looked at those options that would not significantly increase the length of the instrument. One way to do this is to keep the free-flight distance the same as in the two-stage case. This method would maintain the long and surface roughness-tolerant working distance of the two-stage LAMS reflectron. Increasing the number of stages, in a computer model with this geometry, produced mixed results. The energy

range of focusing was indeed increased, provided the grid positions of the higher-order stages were in exactly correct positions. However, if the reflectron length was also kept constant, some of these grids had to be spaced very close together to define the subtle potential variations required. In the case $N=6$, some grids were only separated by a mm or so. Tolerances on these spacings (across the whole grid surface) were quite close, possibly beyond the feasibility limit for remote operation. In addition, while the resolution with the multi-stage reflectron does increase somewhat in theory, the gains cannot be fully realized in practice. The laser ablation event produces ions that form at a range of times and positions. This range sets an average lower bound on peak widths of about 40 ns in LAMS. As such, the model narrowing of TOF dispersion from say, 50 ns to 10 ns, has limited use. A second model permitted the extension of the reflectron, from 4.0 cm to 8.1 cm, but with the free-flight distance still constant. In this geometry, the grids were spaced by no less than 1 cm each, giving an energy window of $V_A = 0.27 V_0$, for the six-stage model.

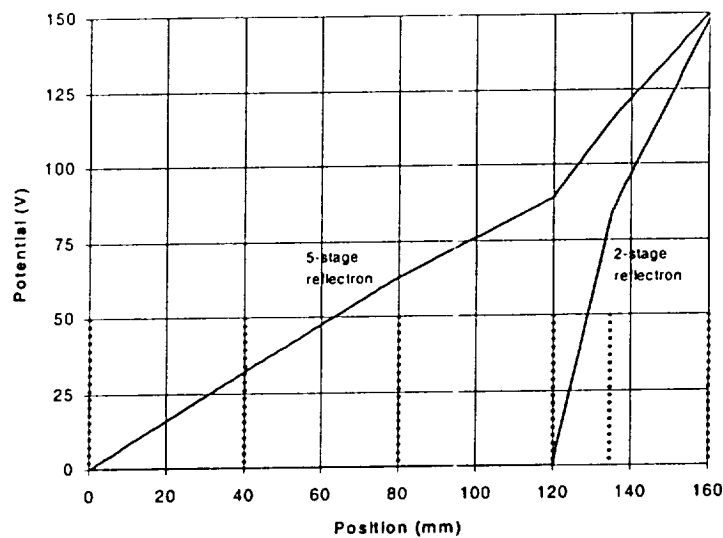


Figure 2 - Configuration of tested five-stage reflectron compared with standard 2-stage LAMS design. Vertical dashed lines denote grid positions.

One higher-order reflectron ($N=5$) with a shorter free-flight distance was implemented in hardware. This model was chosen because it only required a simple modification to LAMS, without extending the overall length (which would have required a longer vacuum chamber). Two additional grids were placed in the region between the detector and the previous reflectron, dividing this region into three field segments of 4 cm in length (Fig. 2). When these grids were grounded, the instrument was equivalent to the original two-stage LAMS configuration, allowing direct comparisons. We are continuing to analyze this modification, but initial results indicate that for targets with widely-separated elements (such as the Co-W carbide mentioned), strong peak tailing, observed in wide-window spectra with the two-stage reflectron, can be substantially improved with the additional grids (Fig. 3).

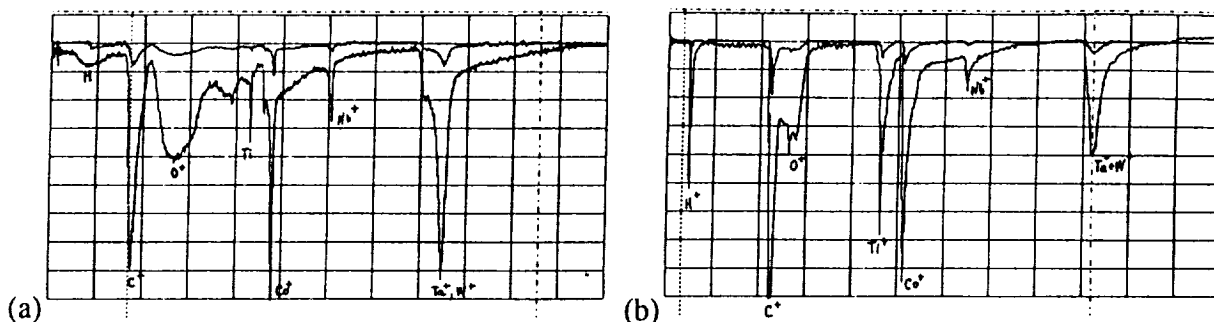


Figure 3 – Wide-window (0,150) V single-shot LAMS spectra of Mo-W carbide target. Low- and high-gain signals differ by a factor of 10. (a) Two-stage reflectron (other grids grounded), including ions below $V_f = 90$ V. (b) Five-stage reflectron, with grids at 0, 32, 63, 89, 115, and 150 V, above the detector (additional grids spaced by 4 cm).

2.1.2 Sample Type Variations

The purpose of analyzing a range of sample materials with LAMS is to determine the matrix dependence of individual elemental and isotopic yields, and to establish the capabilities for grain-to-grain analysis in heterogeneous samples. In ideal (model) conditions, a high irradiance laser pulse incident on a flat, highly absorptive surface produces a plume of singly-charged atomic ions with abundances in proportion to those in the material sampled. For materials fine-grained enough for a single pulse volume ($50 \mu\text{m}$ diameter \times $0.5 \mu\text{m}$ depth, or $\sim 10^{-9} \text{cm}^3$) to sample the bulk, it would be sufficient to record a single, representative sequence of spectra.

In real sample materials, several factors contribute to variations from ideal behavior. Paramount among these is the dependence of the ion signal on the sample type itself. We have analyzed pure metals, metal alloys, carbides, and ceramics, all in solid form. We have also examined both solid and powdered/granular forms of glass, rock, soil, and meteorite samples. LAMS has an optimal operating mode for each type of sample, and the determination of the parameters and reproducibility of these modes has been one of the major advances in the development of LAMS toward eventual analyses of unknown materials *in situ*.

Primarily metallic materials in solid form (disks and foils) produced ions with higher kinetic energies than other targets, on average. These materials also showed the strongest mass-dependent fractionation (with higher mass sensitivities increased up to 20-fold in energy windows above 150 eV). In addition, metals required a longer equilibration period than other types – the intrinsic steady-state reproducibility was attained only after several dozen laser shots in place at low-to-moderate irradiance. In energy windows above 150 eV, metal target reproducibility was rather poor, partly due to the highly-variable sensitivity there. However, between 80 and 110 eV, for approximately 1GW cm^{-2} irradiance, reproducibility in NIST SRM steel standards was excellent, with standard deviations below 5%.

Spectra from solid rock and meteorite samples were also fractionated toward higher masses, though the relative sensitivities were more reproducible, and isotopic precision (from relative variations in neighboring masses) was significantly improved over metals. A clear example of this improvement was demonstrated with a terrestrial desert basalt. Figure 4 shows a typical

narrow-window spectrum and Ti isotope data for 22 laser shots. The minor Ti isotopes were accurate to within 5%, with a clear sensitivity trend increasing with mass. Energy spectra with rocks and meteorites were comparable to, but slightly lower on average than those for metals. In these much more heterogeneous targets, we found that distinct compositional regions could be identified simply by observing the abundance ranges of several elements. Most distinctive were the rapid onset of Fe/Ni-rich mineral grains within a carbonaceous meteorite. LAMS detects total Fe atomic abundance, and is not likely to be biased toward either Fe oxides pure Fe metal at ablation irradiances. As such, Fe was seen in nearly all spectra, but within the “grains” the Na, Mg, Al, and Si peaks were highly attenuated, while S, Fe, and Ni abundances were high and reproducible. Such grains were “burned through” in dozens laser shots, which at 0.1 - 0.3 $\mu\text{m}/\text{shot}$ is consistent with grain sizes of tens of microns. The presence of troilite grains (nearly stoichiometric FeS) is a characteristic of meteorites, and a possible indicator of sulfide deposits.

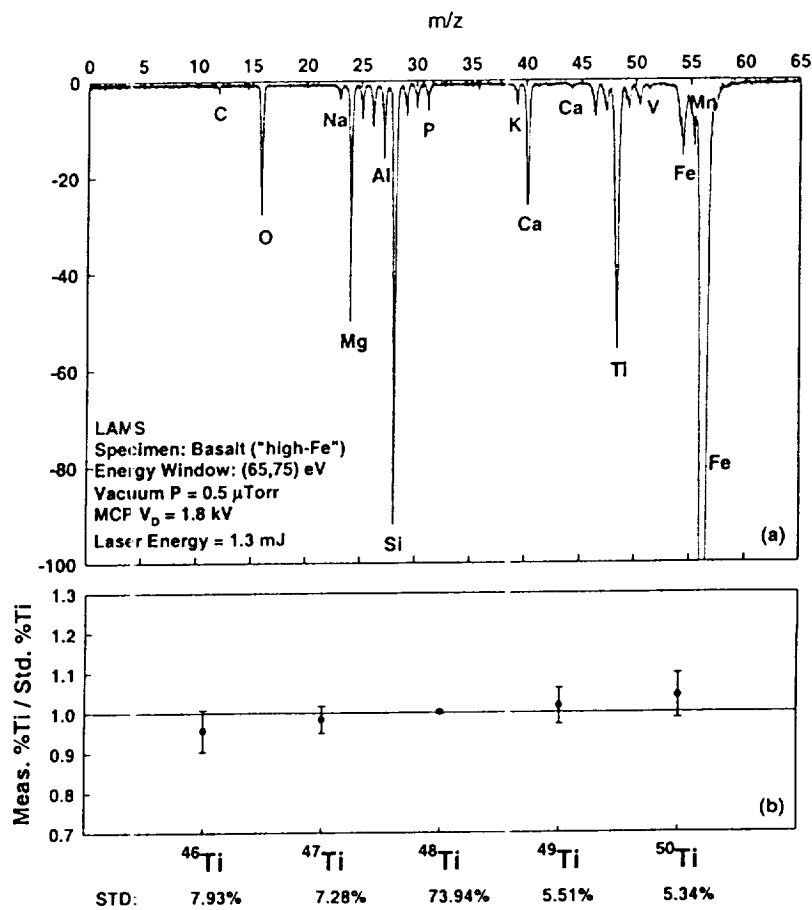


Figure 4 – LAMS data for terrestrial desert basalt. (a) Single laser shot spectrum in energy window (65,75) eV. (b) Raw integrals of Ti isotope peaks as percentage of total signal from m/z 46 through 50, compared to standard terrestrial values.

An important third class of sample types analyzed were loose powders and soils, and/or pellets pressed from those. Due to the sensitivity of the laser ablation method to surface roughness and possible problems with voids on the size-scale of the laser spot, it was somewhat surprising that reproducible spectra were obtained from loose targets. Initially, we observed that these samples gave very weak signals in the normal energy range (above 100 eV). Quantitative measures were impossible in this range because the high laser power required to get enough signal also produced copious doubly-ionized peaks and extensive peak tailing. Eventually, we found that ions were formed reproducibly, but with much lower kinetic energies than observed in solid samples. Mean energies ranged from 30 to 50 eV, depending on the sample. At these lower energies in soils and powders, the laser power needed for good signal-to-noise ratio spectra was lower than with solids (rock or metal) in the same energy range. Bulk analysis is thus more readily achieved with these targets, by defocusing the laser (to 100-200 μm diam.) to average over several grains, rather than relying solely on shot sequences. This behavior is very encouraging for *in situ* reconnaissance, where rapid assessment of bulk elemental abundances at low power can help decide whether to spend more resources to study the sample at smaller scales.

A single-shot (74,85) eV spectrum from the Mars soil simulant JSC Mars-1 (provided by C. Allen of Lockheed-Martin Corp., Houston TX) is shown in Figure 5. This sample contains a distribution of oxides similar to compositions derived from Viking and Pathfinder studies [Allen *et al.*, 1998]. It has been quite valuable for analyzing LAMS prospects with pertinent soil samples. Fluctuations between compositional regions were less distinct than in solid targets, but spectra could be broadly categorized into low and high (Ca+Ti)/Si regions. (Figure 5 is high.) This behavior is consistent with independent XRD data showing the presence of two particle types, one of which is dominated by both Ca-feldspar and Ti-magnetite [Allen *et al.*, 1998].

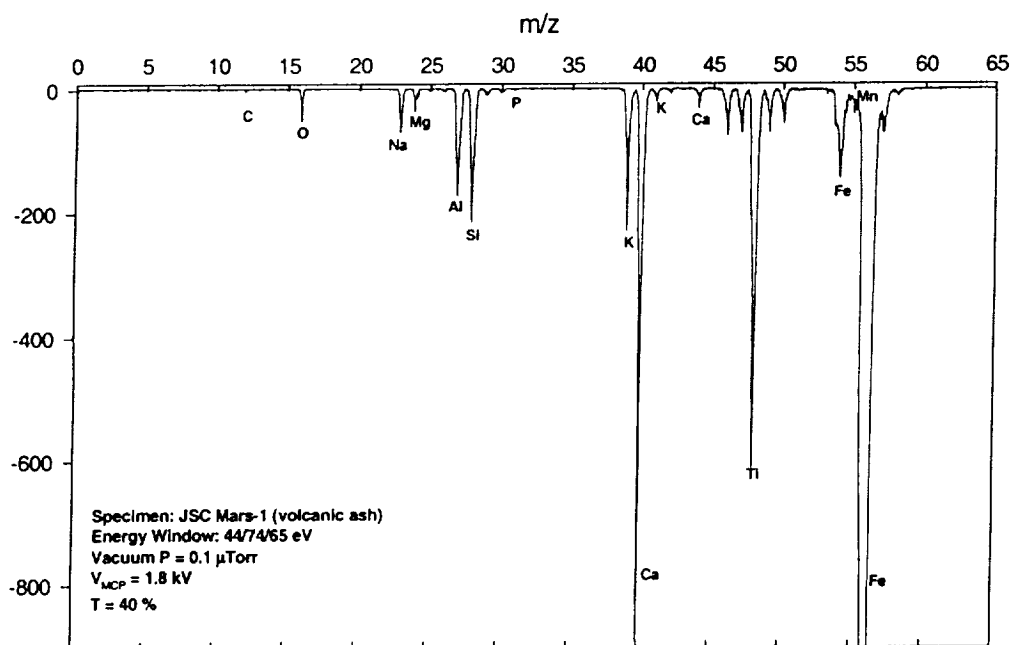


Figure 5 – Single shot LAMS spectrum from pressed pellet of JSC Mars-1 volcanic ash Martian soil simulant, recorded after 10 shot “warmup” on fresh surface.

A comprehensive comparison between the behavior of solid and powdered target materials and the prospects for broad classification of extraterrestrial rocks from elemental analyses is ongoing, and will be described in an upcoming article.

2.1.3 Elemental Analysis and Mineralogy

Whether on a complex world like Mars or Venus, or on an undifferentiated small body with no atmosphere, composition information at the elemental, molecular, and mineralogical levels will be desired from an *in situ* probe. These three areas of information are crucial to begin to understand the geological and organic (possibly biological) processes that the body has undergone. They are also critical to determine which samples will be cached for return to Earth. Complete robotic analysis of a macroscopic sample on all three levels is very difficult, however. Just the sample preparation step to access unweathered rock materials, or core samples, and to find, prepare, and load the sub-parts of those containing the desired minerals is trouble enough. Once a sample, say a cleaved rock chip obtained by a drill, is obtained and positioned in an instrument, it would be extremely useful to get a rapid, broad, "first-order" characterization of various parts of the chip surface. This would permit us to assess whether the sample is similar to previous samples, and to decide whether to expend precious further resources to do a complete characterization.

The LAMS device can fill this role very effectively in a suite containing a range of chemical and mineralogical tools, including APXS, GRS, neutron, Raman, and XRD/XRF. The APX, GR, and neutron activation spectrometers can do bulk chemical analysis of many elements on a sample before it is extensively handled (or loaded into a vacuum chamber). This type of analysis represents the centimeter-scale end of chemical composition studies on scales ranging from a few centimeters to a few kilometers. These instruments have performed capably in the past (e.g., APXS on Mars Pathfinder) and are carried on missions currently flying (e.g., NEAR X/GRS). Bulk measurements, particularly coupled with spectral reflectance, can provide important insights into the mineralogy of a planetary object. They are not, however, capable of directly determining the mineralogy and, by inference, the petrogenesis of a planetary rock or body. A striking example of this is the S-free rock composition determined by the Mars Pathfinder APXS. While the calculated bulk composition is similar to that of the volcanic rock andesite, the lack of high spatial resolution measurements of the mineralogy and composition of these rocks severely limits our ability to determine the genesis of this rock.

To obtain chemical analysis that is correlated with grains seen in an imager FOV, the laser probe capability of LAMS is then required. While mineralogy is ideally determined by examining the crystal structure of a mineral by X-ray diffraction, in practice, the chemical composition of the mineral is diagnostic of the mineralogy. In this mode, chemical analyses of individual minerals using TOF-MS is equivalent to determining the mineralogy of a meteorite using the electron microprobe. The key question is whether the TOF-MS has both the spatial resolution needed and the ability to determine the key elements for mineralogical analyses.

The 30-50 μm spatial resolution of LAMS is more than adequate for the analyses of all but the finest-grained extraterrestrial materials (e.g., cosmic dust, some carbonaceous chondrites, and

some cometary materials). Grain sizes of metamorphosed chondrite, partially-melted asteroidal rocks, asteroidal basalts, and Martian meteorites are all on the scale of 100 microns or more and are easily analyzed with LAMS. (For example, a 1 cm section of the Martian meteorite Zagami is shown in Figure 6.) To distinguish a range of minerals likely to occur in asteroidal and Martian rocks (not the soils, but the bedrock), the key elements include Si, Al, Ca, K, Na, Mg, Fe, P, S, Ni and O. This could yield identification and compositions of plagioclase (Ca,K,Na,Al,Si,O), pyroxenes (Ca,Mg,Fe,Si,O), olivine (Fe,Mg,Si,O), phosphates (Ca, P, O), metal (Fe,Ni) and sulfides (Fe,S). By creating surface element maps at the scale of grains, within the current accuracy limits alone, LAMS can reveal the probable identity of each grain and the contextual relationship to other grains, which can limit the range of formation mechanisms of the sample rock. It can also probe the interiors of calcium-aluminum inclusions (CAIs) and chondrules.



Figure 6 - Magnified surface view of the Martian meteorite Zagami. The width is 1 cm and grains are > 100 µm across. The small centered dot is a simulated 50 µm laser spot

Work with whole rock samples, as described above and in previous reports [e.g., Brinckerhoff *et al.*, 1998b], has demonstrated, in a preliminary way, the ability of LAMS to use both bulk elemental data and shot-to-shot fluctuations to characterize extraterrestrial materials *in situ*. We have continued this analysis with a new meteorite provided as a sample blind into the LAMS vacuum chamber. The sample, which was only viewed through the LAMS optics, was a powdered or granular matrix of uniform, light color. A distribution of grain sizes was evident across the loosely-packed surface in the sample holder. The elemental distribution in the mass range m/z 12 - 65 was quite different than the previously-analyzed CM2 chondrite [Brinckerhoff *et al.*, 1998a]. The sample clearly contains a wider variety of distinct compositional regions, most of which are marked by a higher ratio of transition metal to silicon abundances. Whereas the CM2 chondrite contained a reproducible "matrix" with minor Ni/Fe-rich inclusions, the new sample contained a Mg-Si and Ca rich phases punctuated by sequences of shots with almost entirely S and Fe, and by an additional rare component with Cr, Fe, Ni, and Cu. These observations must of course be taken in the context of the homogenization of the sample by the powdering process (the laser may sample several grains at once).

Example spectra from these types are shown in Figure 7. Spectrum (a) is typical of the Si-Mg-Ca type, with a minor S contribution and higher Mg:Si than seen in the CM2 chondrite. In (b), the S abundance is dramatically higher, and the Ca signal has almost disappeared, relative to Si. In (c), the spectrum is dominated by Fe and S, while the (now minor) Mg:Si ratio remains approximately the same as in (a). Spectrum (d) shows an example of the rarer “metal-rich” spectrum in which Cr, Fe, Ni, and Cu (and minor Na and K) made up nearly the entire ion flux. The appearance of these grouped elements seemed to be anti-correlated with the presence of S. Cu in particular is a minor element in many meteorites, but its occurrence in this group and at this level may be consistent with a chondritic material. Further work will help determine if this consistency bears out.

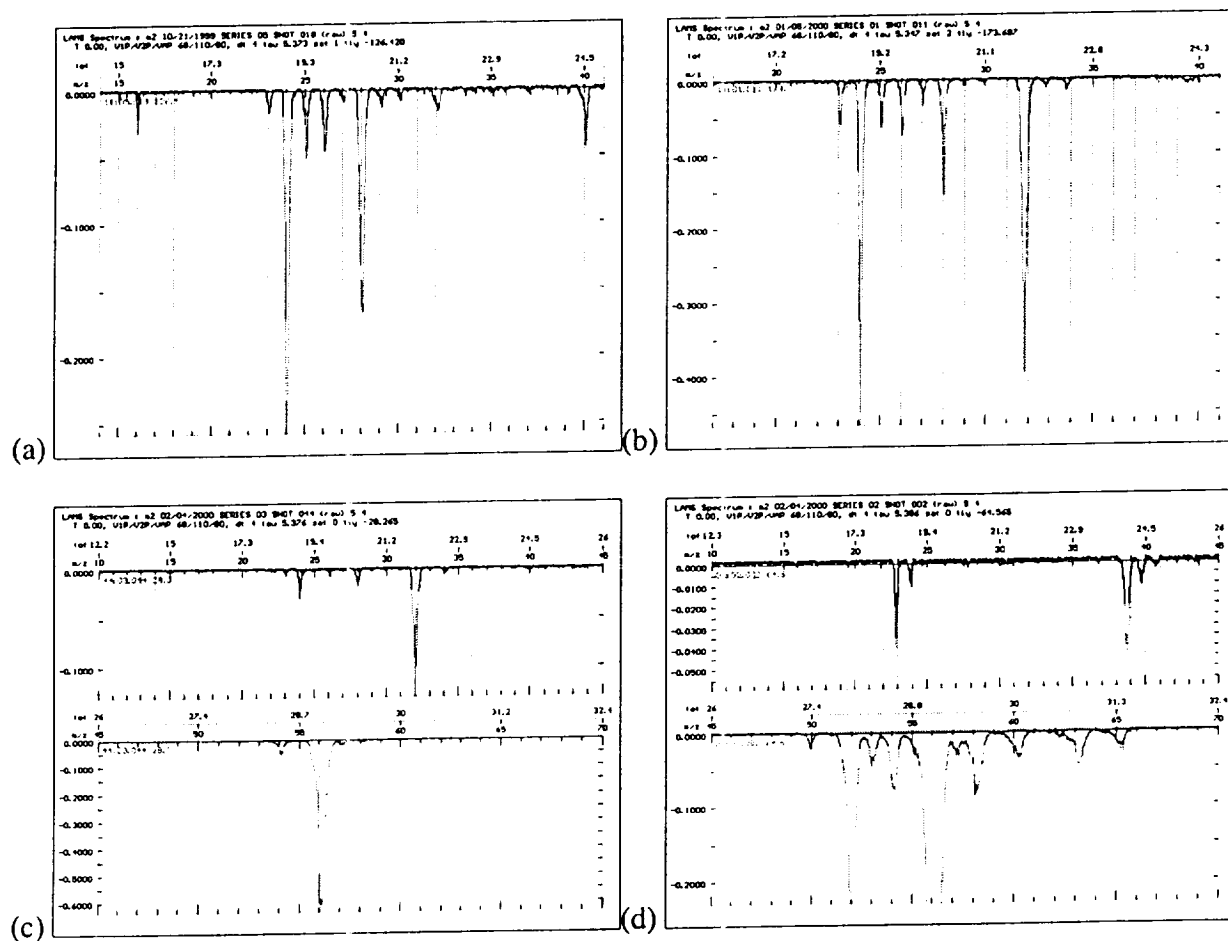


Figure 7 - Single laser shot LAMS spectra from powdered meteorite sample blind, loosely packed into sample holder. (a) Typical of high-Mg,Si,Ca; low K,S shots. (b) Similar to (a) but with stronger S peaks and vanishing Ca peak. (c) Typical of spectra dominated by Fe and S. (d) Rarer type of spectrum dominated by transition metals from Cr to Cu, and containing some Na and K.

2.2 Instrumental Analysis

In addition to analyses of various samples with LAMS, we have also examined some aspects of the instrument design and operation, with an eye toward eventual improvements in performance and reductions in size and mass. We mention a few here for their pertinence to the current state of development and an understanding of intrinsic performance limits, noise, and design options.

2.2.1 Reflectron Modeling

A simple, two-dimensional model of LAMS in SIMION has permitted us to test the basic characteristics of proposed ion optical modifications before they are implemented in hardware. The model has reproduced the major characteristics of LAMS quite faithfully in terms of the reflectron focus, the lateral ion velocity fractionation, and the dependence of resolution on the free-flight distance. Figure 8 shows the paths of ions of masses 100, 101, and 102 amu emitted with a range of kinetic energies between V_A and V_2 . Trajectories for ions with two different initial angles from the center axis are shown. Spatial positions of ions at 2 μ s intervals are indicated for clarity. The clear spatial separation of masses into distinct packets is evident as the population approaches the detector.

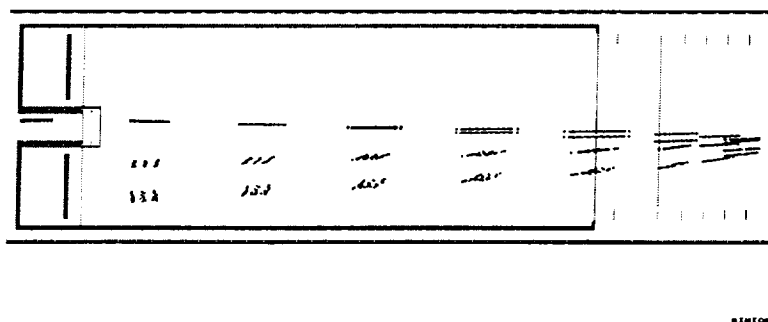


Figure 8 – SIMION model showing 2 μ s snapshots of ions with masses 100, 101, and 102 amu emitted with different initial angles and velocities. The additional lens element centered over the detector aperture (left side) was introduced to test enhancements from collimation and beam steering.

One effect seen in this model that was missed in one-dimensional calculations is the effect of the spaced-reflectron rings on ions as they slowed and reflected. Ions with greater lateral velocities approached the rings more closely and were proportionately more disturbed by non-uniformities in the electric field. This led to those ions being more dispersed in TOF at the detector. We are currently examining what possible fractionation could arise from this via mass effects in the initial velocity distribution and in the lateral forces in the reflectron. We have also been able to examine the fate of particles with energies too low to pass through the analytical grid. Ions with

small initial angles can actually survive through twenty or more reflections between the grids in the flight tube before they collide with the side of the tube. These “rejected” ions represent the vast majority of particles in the flight tube, and they are likely fractionated toward lower masses due to the intrinsic kinetic energy distribution of ablation. As such, the possible interference between these ions and those within the energy pass band has been of some concern. We are currently adapting the model to calculate the impact factors between incident and reflected ions, to determine the magnitude of this interaction. A simple model modification that reduces the number of reflections was to introduce a slight angle in the analytical grid, sloping away from the center axis. Reflected ions are given a finite lateral velocity component, while transmitted ion trajectories are mostly corrected by the symmetrical nature of the $0-V_A-0$ assembly. Unfortunately, this modification is not so simple to implement, but may be worth pursuing if the numerical studies prove significant.

2.2.2 Grid Effects

Another small but significant interfering effect related to reflected ions was initially mistaken as evidence for spurious appearances of trace element and/or molecular cluster peaks. However, these peaks were diffuse and did not usually fall on unit mass numbers. A detailed analysis of these “echo” peaks revealed that they arrived at a constant multiple (1.77) in *time* from certain base peaks. Figure 9 shows the effect for hydrogen in the window (18,25) eV, for which is was most reproducible. The hydrogen and deuterium peaks occur at the expected positions and in the expected ratio. The diffuse peak at approximately 14.2 μ s represents a signal approximately 10^{-4} times the ^1H peak, or slightly less than ^2H , although this ratio varied somewhat when observed for other elements, and would be a limitation on abundance sensitivities. This is because the extra peak may interfere with small peaks nearby, and because the signal cannot be “assigned” to the abundance of a known element.

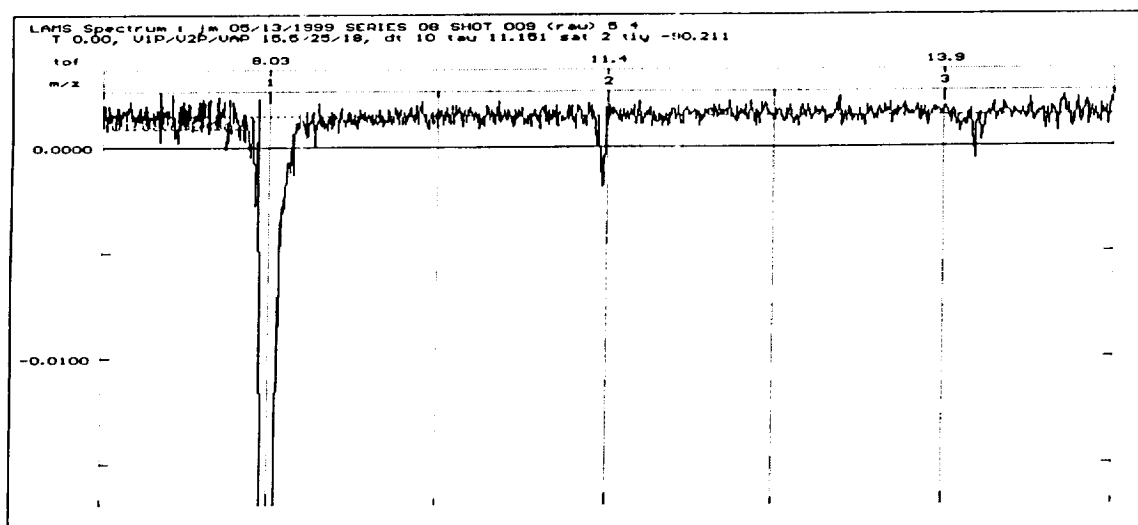


Figure 9 – Example of a spurious “echo” peak in the signal of atomic hydrogen.

The use of the term “echo” is somewhat leading, of course, as we eventually determined that a small fraction of ions *within* the energy pass band can still be reflected nearly elastically by the wires of the analytical grid. After their return trip through the reflectron, these ions still have

sufficient kinetic energy to pass through to the detector, but will have been defocused. This second “tandem” pass is equivalent to a TOF-MS with a shorter free-flight distance. When this hypothesis was tested in a 1D model (Figure 10), the returning ions arrived at the detector at the original TOF times a mean factor of *exactly* 1.77. Current work on this effect is seeking to understand its seemingly element and/or energy dependent appearance. We are also studying a type of gridless analytical grid assembly that has the potential to eliminate this “parasitic” effect. From another vantage point, we may also be able to use this result to design a “quasi-tandem” instrument wherein the analytical grid is pulsed at a given time to send ions back for second, third, or further passes through the reflectron, increasing the flight distance and possibly the resolution.

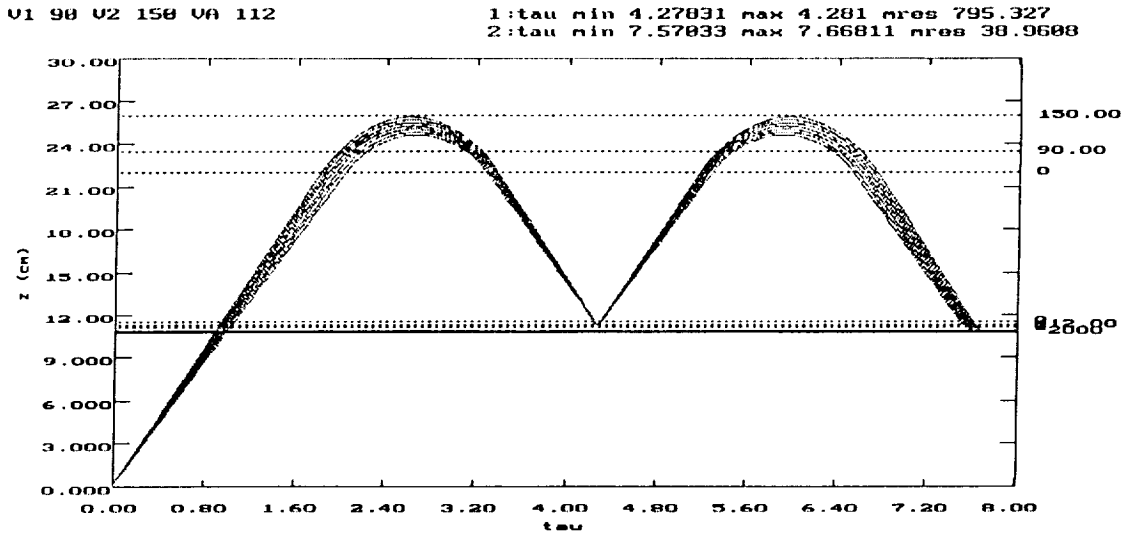


Figure 10 – Model of ions reflected elastically from the analytical grid and returning to the detector at a later time and with lower resolution. The calculated resolution of the reflected ions is equal to that at the point where the ions initially passed through the detector aperture. By lowering the focus voltage V_f , the second-pass resolution can be increased by a factor of ten, at the expense of the first-pass resolution.

2.2.3 Alignment

Another effect we have observed is more of a diagnostic tool to understand the sensitivity of the reflectron is misalignment with the LAMS axis. During periodic reassembly and mounting of the flight tube, we noticed that small changes in the angle between the plane of the reflectron grids and the detector plates could be observed in the shapes of peaks, which occur over the 50 ns time scale of the flight-path difference introduced by the angle. For a relative tilt of θ degrees, the flight-path difference between the edges of a MCP with diameter d cm would be $d \sin \theta$ (about 1.7 mm for $d = 5$ cm and $\theta = 2^\circ$). The difference in flight times across this diameter would be

$$\Delta \text{TOF} = \frac{d \sin \theta}{\sqrt{2E}} \sqrt{m},$$

where E and m are in eV (i.e., $m = 931.5 \times 10^6 / c^2 A$, with c in cm s^{-1} and A in amu). For $d = 5$ cm, $\theta = 2^\circ$, and $E = 100$ eV, we have $\Delta \text{TOF} = 12 A^{1/2}$ ns, which ranges from 12 ns for $A = 1$ to 120 ns for $A = 100$. This scales linearly with angle for small angles, so $\theta = 4^\circ$ will produce a range of 24

ns to 240 ns, etc. In addition to producing this line broadening, the tilt will also introduce a notch in the peak because of the MCP center hole (and surrounding highly-worn region). In other words, the double-peak is an *image* of the plate. This effect is shown in Figure 11, and the correction in the alignment restores the performance (Fig. 11b).

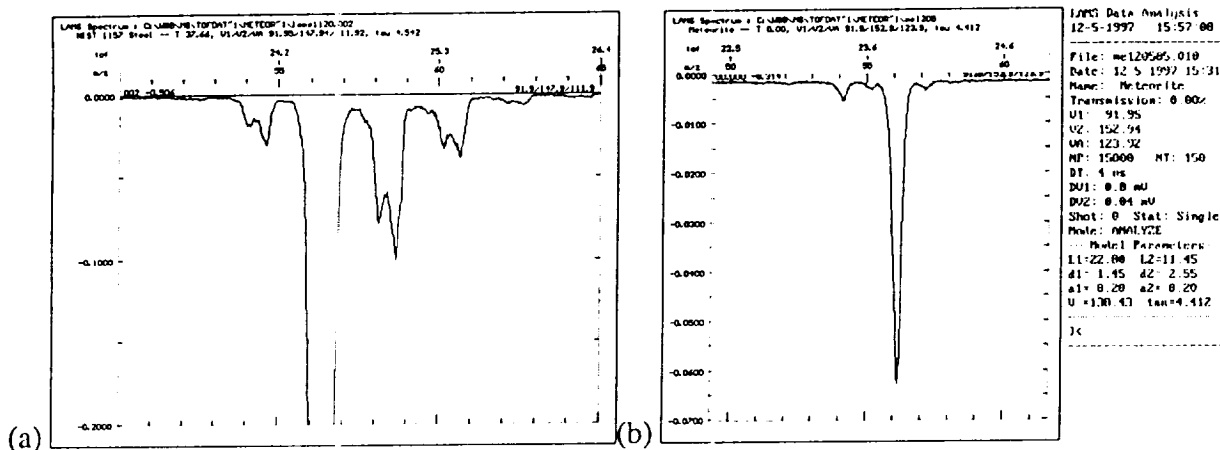


Figure 11 – Behavior of LAMS spectra (a) before and (b) after reflectron alignment.

3. Future Directions

At the present stage, LAMS can provide vital composition data *in situ* on planetary and small body missions. Elemental and isotopic abundance data that are correlated with a magnified image of the sample in question can greatly enhance our knowledge of rock, soil/regolith, and ice composition and mineralogy without expending great resources. To maximize this potential, further measurements on standard and meteorite materials must be conducted, and certain instrument modifications are worth pursuing in the instrument development.

Incorporating an Einzel lens (or other ion lens) will increase the throughput via collimation. In LAMS the position and voltage range of lenses must be carefully adjusted to avoid complications due to the plasma plume. Similarly, a pulsed ion gate will permit the selective suppression of certain TOF regions, to minimize any ion interaction difficulties and increase sensitivity. It too must be reexamined for miniature instrument use. The size limitations in planetary exploration also restrict the flexibility in reflectron design. Tests are currently underway with ideal, or nearly-ideal reflectron designs that correct the TOF over a much wider energy range than the two-stage LAMS unit. High-order correction in LAMS demands component positions and electrostatic parameters be highly precise and robust.

We are also testing devices similar to LAMS with an ultraviolet (UV) Nd:YAG tripled (355 nm) or quadrupled (266 nm) laser that may increase the sensitivity to various species, including molecular compounds. Shorter wavelengths may also produce a smaller and more-reproducible crater. However, any improvement with UV must be weighed against the increased complexity and fragility that may be required in a flight unit. The IR laser was originally chosen to test the simplest LAMS that can provide useful results on future missions.

4. References

- Allen, C.C., K.M. Jager, R.V. Morris, D.J. Lindstrom, M.M. Lindstrom, and J.P. Lockwood, Martian soil simulant available for scientific, educational study, *EOS* 79, 405, 1998.
- Brinckerhoff, W.B., A.F. Cheng, R.W. McEntire, and G.G. Managadze, Miniature laser ablation time-of-flight mass spectrometer, in *Lunar and Planetary Science XXIX*, Abstract #1789, Lunar and Planetary Institute, Houston, 1998a.
- Brinckerhoff, W.B., R.W. McEntire, A.F. Cheng, and G.G. Managadze, Laser ablation time-of-flight mass spectrometer for elemental and isotopic analysis, in *Third IAA International Conference on Low-Cost Planetary Missions*, Preprint #IAA-L98-1106, International Academy of Astronautics, Pasadena, 1998b.
- Brinckerhoff, W.B., G.G. Managadze, R.W. McEntire, A.F. Cheng, and W.J. Green, Laser time-of-flight mass spectrometry for space, *Rev. Sci. Instrum.* 71 (2), 536, 2000.
- Cotter, R.J., *Time-of-Flight Mass Spectrometry*, American Chemical Society, Washington, 1997.
- Meyer, C., A.H. Treiman, and T. Kostiuk, eds. *Planetary Surface Instruments Workshop*, LPI Tech. Rpt. 95-05, Lunar and Planetary Institute, Houston, 1996, 115 pp.

Appendix A

Reprint attached [Brinckerhoff *et al.*, 2000].

Laser time-of-flight mass spectrometry for space

W. B. Brinckerhoff^{a)}

Applied Physics Laboratory, The Johns Hopkins University, Laurel, Maryland 20723-6099

G. G. Managadze

Space Research Institute (IKI), Moscow, Russia

R. W. McEntire, A. F. Cheng, and W. J. Green

Applied Physics Laboratory, The Johns Hopkins University, Laurel, Maryland 20723-6099

(Received 5 April 1999; accepted for publication 20 October 1999)

We describe a miniature reflection time-of-flight mass spectrometer for *in situ* planetary surface analysis. The laser ablation mass spectrometer (LAMS) measures the elemental and isotopic composition of regolith materials without any sample preparation or high-voltage source extraction. The small size ($<2 \times 10^3 \text{ cm}^3$) and low mass ($\sim 2 \text{ kg}$) of LAMS, due to its fully coaxial design and two-stage reflectron, satisfy the very strict resource limitations of landed science missions to solar system bodies. Microscopic surface samples are obtained with a short-pulse laser focused to a spot with a diameter $\sim 30\text{--}50 \mu\text{m}$. Coupled with a microimager, LAMS can interactively select and analyze a range of compositional regions (with lateral motion) and access unweathered, subsurface materials (with repeated pulses). The mass resolution is sufficient to distinguish isotopic peaks at unit masses, and the detection limits are on the order of a few ppm. The design and calibration method of a prototype LAMS device is given, including the development of preliminary relative sensitivity coefficients for major element bulk abundance measurements. © 2000 American Institute of Physics. [S0034-6748(00)00602-X]

I. INTRODUCTION

As the exploration of the solar system expands in depth and scope, the demand for miniature, yet fully capable, analytical instrumentation for space will increase. Mass spectrometers in particular, which can provide a complete chemical composition of all phases of matter, will continue to play a central role in orbiting,¹ descent,² and landed³ planetary missions. Several types of mass spectrometers for space, including sector, quadrupole, and time-of-flight (TOF) instruments, have been successfully flown or are under development. One of the major challenges for mass spectrometry in the next generation of landed missions to planets and small bodies will be the necessity to robotically analyze materials from a range of geological contexts. This *in situ* requirement will call for instruments with simple, robust design, little or no sample preparation, highly sensitive detectors, and a wide mass range. This last factor will be especially important for bodies such as Mars, Europa, and certain small bodies, where the detection of organic molecules may be a key scientific goal.

TOF-mass spectrometry (TOF-MS) is a particularly promising technique for *in situ* science. Gas-phase ions are detected with minimal attenuation compared to mass filters. Mass resolution and sensitivity are, in principle, independent of mass. The mass range is bounded only by the limits of detectability and recording time. Additionally, TOF-MS is ideal for analysis of solids due to its low sample usage, rapid, multichannel detection, and natural coupling with pulsed desorption. These features reduce the problem of elemental

fractionation observed in mass-scanning techniques. However, before the 1980s, the power of TOF-MS was limited by a broad temporal spread of ion formation (i.e., lack of a good "zero" time) and slow electronics. With the advent of short-pulse lasers and high-speed transient digitizers over the past two decades, these major limitations have been mostly overcome and TOF-MS is experiencing a renaissance in the analytical community.^{4,5} The development of miniature TOF-MS for space applications has thus entered a period of optimistic growth.

TOF-MS instruments detecting energetic ions and neutral atoms have flown on several missions, but have yet to be successfully deployed for surface analysis. The Russian PHOBOS mission carrying LIMA-D, a TOF-MS designed to study the surface of Phobos from a hovering distance of 30–80 m, unfortunately failed to reach its objective.⁶ Current efforts, such as use of the laser ablation mass spectrometer (LAMS) described in this article, primarily focus on lander or rover deployment scenarios. In the LAMS technique, the spectrometer is positioned over a microscopic field of view, chosen interactively with an optical imager, and a small volume of surface material is then evaporated and ionized with a pulsed laser. On atmosphereless bodies such as asteroids, no sample contact is required and forward contamination is eliminated. On bodies with an atmosphere, a minimal interaction is required to bring material into a vacuum chamber, but no further contact would be required by LAMS.

Following a description of the LAMS instrument and its operation in Sec. II, we present results for some different target materials, and discuss the process of abundance calibration for *in situ* quantitative analysis.

^{a)}Electronic mail: william.brinckerhoff@jhuapl.edu

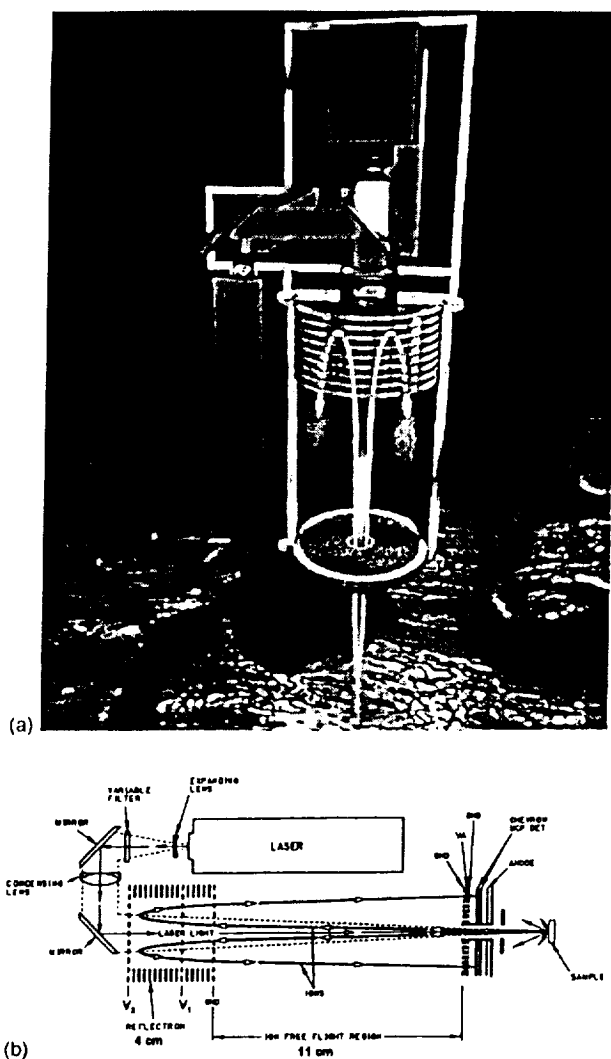


FIG. 1. (a) LAMS shown in orientation for *in situ* sampling, with a cutaway showing the internal design. (b) Instrument schematic. An ~ 8 ns pulse from the Nd:YAG laser is expanded, collimated, and directed through a focusing objective into the flight tube. The laser passes through the grids of the two-stage reflection, the free-flight region, and the hole in the center of the analytical grid/detector assembly to a focused spot of interest on the surface. Positive ions travel up through the same hole, are repelled by the reflector, and strike the active surface of a microchannel plate at a sequence of times proportional to the square root of their mass-to-charge ratios.

II. EXPERIMENT

A. Laser ablation and ionization

The sampling method of LAMS is straightforward (Fig. 1). A Q -switched Nd:YAG laser, with infrared wavelength $\lambda = 1064$ nm and pulse duration $\tau = 8$ ns, is focused to a 30–50 μm diameter spot on the target surface *in vacuo*. In the laboratory system, small chip or pressed powder pellet targets (~ 2 mm across) are mounted on the end of a coaxial linear/rotary motion feedthrough (MDC K075-BRLM). The nominal operating pressure is 2×10^{-7} Torr. The position of the spot is chosen visually with a high-resolution camera that shares the laser's objective lens. A variable attenuator⁷ is used to control the irradiance I , normally between 0.5 and 5 GW cm^{-2} . In this range, the primary sampling process is

ablation, wherein material is evaporated and ejected from the target surface at a high rate, forming an expanding plume. During ablation, molecular structures are dissociated into their atomic constituents, and these vaporized atoms are subsequently ionized as they leave the surface during the laser pulse.⁸ Ionization occurs with varying efficiency and degree at ablation irradiances. It is desired to operate with a maximal, uniform ionization fraction (occurring at higher I) across all elements to best represent the abundances in the analyte.^{9–12} However, for the same reason it is also desirable to minimize production of multiply ionized atoms (also increasing with I), which can cause isobaric interferences in the time-of-flight detection. For instance, doubly ionized iron $^{56}\text{Fe}^{2+}$ will interfere with singly ionized silicon $^{28}\text{Si}^+$. This trade-off is not unduly restrictive. Empirically it has been found that laser irradiances of 1–2 GW cm^{-2} generate mostly singly charged ions with reproducible efficiency and sensitivity throughout the periodic table.⁹

Ablated ions leave the target surface with a distribution of kinetic energies ranging up to hundreds of eV. This distribution naturally depends on the laser power density and material composition, but is expected to remain constant for a given ionic species in a given specimen under fixed conditions. (The meaning of “fixed conditions” is discussed below.) In contrast with most laser time-of-flight instruments, LAMS does not “extract” ions from the target region by pre-accelerating them through a high potential difference. The purpose of extraction in other instruments is to increase the number of ions reaching the detector (via collimation) and to increase resolution by decreasing the relative spread of ion kinetic energies with respect to their mean energy. For example, in matrix assisted laser desorption/ionization (MALDI), the target backplate is set at a several kV positive potential with respect to a nearby grounded grid to extract low-abundance, high-mass species.¹³

In LAMS, the plasma plume generated at ablation irradiances tends to shield external fields from the ion source region, which would reduce the intended benefits of any pre-acceleration.^{14–16} Furthermore, pre-accelerated ions have shorter flight times that can strain the temporal resolution requirements in a miniature instrument. It is also generally desired to avoid high voltages and related design complexities and restrictions to permit laser ablation of unprepared surface materials in a direct, flexible fashion. LAMS is therefore designed to accept the natural kinetic energy distribution arising from the plume, and approaches the mass resolution issue solely through the use of ion energy focusing and windowing (see below). Low-energy analysis of the kinetic energy distribution of ablated ions under various conditions has proven to be useful for the understanding of matrix effects, selective fractionation, and ion interactions. Such information is vital for determining the optimal operating procedure for unknown specimens on remote missions, where high efficiency is required.

Ions with trajectories within approximately 3° from vertical pass through a hole in the center of the detector assembly and enter the LAMS flight tube (Fig. 1). These ions continue up in a field-free region until entering a coaxial reflector (described next), where they experience a repel-

ling field due to grids at fixed electrostatic potentials. A fraction of the ions are turned around and impinge upon the active detector surface. The compactness of LAMS is partly due to this "fully coaxial" design. That is, the optical path of the laser and camera goes along the flight axis, *through* the reflectron grids, and through the centered hole in the detector assembly, normal to the target surface. The interaction between the defocused laser and the grids of the reflectron is negligible.

B. Energy focusing and windowing

The configuration of LAMS is similar to that of the LIMA-D and LASMA instruments.¹⁴ Ions travel from the target surface through a time-of-flight region and are detected by a dual microchannel plate (MCP) assembly at a sequence of times proportional to the square root of their mass-to-charge ratios. That is, $\text{TOF} \propto (m/z)^{1/2}$ for a given ion with mass m and positive charge z . The constant of proportionality depends of course on the initial energy of the ion and the particular path it takes through the spectrometer. It is generally desired to arrange for this constant to be the same for a given m/z over a wide range of energies, so that ions with the same mass arrive at the detector simultaneously. LAMS achieves such energy focusing with a second-order electrostatic ion mirror, or reflectron. As shown in Fig. 1, the reflectron consists of a stack of rings that define the above-mentioned repelling field. Mesh grids across three of these rings serve to divide the reflectron into two constant-field regions. The lowest grid is at ground, while the upper two are set at adjustable potentials V_1 and V_2 .

Now, whereas in the field-free, or free-flight, region the TOF varies with energy as $E^{-1/2}$, in the reflectron region the TOF varies as $E^{+1/2}$. By tuning the field profile in the reflectron via the grid voltages V_1 and V_2 , the time-of-flight dispersion at the position of the detector can be nearly eliminated over a wide energy range. Specifically, ions with higher E penetrate more deeply into the repelling field of the reflectron, and the extra time they spend in the reflectron permits lagging, lower-energy ions to "catch up" by the time the entire packet reaches the detector. The presence of the first stage grid V_1 simultaneously permits a wider range of energy focusing and allows the reflectron to be significantly shorter than the free-flight region. This means a miniature instrument can accommodate laser focusing over a rough surface and maintain high performance. The minimum free-flight distance is actually set by the necessary separation between the reflectron and the detector. In the LAMS laboratory development system, the reflectron length is only 4 cm, while the free-flight distance is 14–22 cm. As part of the free-flight distance is external to the flight tube, a flight version of LAMS is estimated at <20 cm total length.

The mass resolution R is determined by the temporal width of the arriving packet of ions with a given mass, relative to the time interval before arrival of the next mass. Equivalently, it may be expressed as $R = m/\Delta m = t/(2\Delta t)$, where Δt is the temporal width (say, at half maximum) of the ion packet and t its mean time of flight. To achieve "unit" mass resolution, where peaks at neighboring mass

numbers do not interfere,¹⁷ R should be in excess of 250 (achieved by LAMS). For free flight only, this would translate into a restriction on initial kinetic energy width of $\Delta E/E < 1/500$ but, with its two-stage reflectron, LAMS improves this to $\Delta E/E \leq 1/4$.

In practice, LAMS samples an energy band from the full distribution that is narrower than this theoretical limit. This is accomplished with a discrimination, or "analytical" three-grid assembly placed in front of the detector. The top and bottom grids are grounded, and the voltage V_A on the center grid is set such that $V_1 \leq V_A \leq V_2$, defining an acceptance window between V_A and V_2 . As such, only ions that reach the second stage of the reflectron ($V > V_1$) are detected. This windowing is desired to prevent unfocused ions from reaching the detector. In the present geometry the optimal focus is found at approximately $V_1 \approx 0.6V_2$ (see below), below the range where the reflectron TOF versus energy curve varies significantly.

Spectra are recorded by digitizing the current output of the MCP as a function of time after the laser pulse. TOF spectra are automatically converted into mass spectra using a scale coefficient calculated from the instrument dimensions and grid voltages. Neglecting the initial temporal and spatial spread of ions, as well as interactions between them, the LAMS TOF-to-mass scale for a particle with mass m and initial kinetic energy zV is given by

$$\left(\frac{2z}{m}\right)^{1/2} t = \frac{L_1 + L_2}{V^{1/2}} + \frac{4d_1}{V_1} [V^{1/2} - (V - V_1)^{1/2}] + \frac{4d_2}{V_2 - V_1} (V - V_1)^{1/2} + \frac{2(a_1 + a_2)}{V_A} [V^{1/2} - (V - V_A)^{1/2}] + \frac{2a_3}{|V_D|} [(V - V_D)^{1/2} - V^{1/2}], \quad (1)$$

where L_1 and L_2 make up the total free-flight distance (surface to reflectron, reflectron to detector), d_1 and d_2 are the lengths of the two reflectron regions, a_1 and a_2 are the distances separating the analytical grids, a_3 is the distance from the lower ground grid to the upper MCP, and V_D is the (negative) potential across the MCP. The accuracy and reproducibility of this scale are sufficiently high that calibration corrections are not required.

Neglecting the last two terms, as $(a_1 + a_2)/V_A$ and $a_3/|V_D|$ are small, and writing $c = V_1/V_2$ and $p = V/V_2$, the TOF expression may be approximated by

$$V_2^{1/2} \tau/L \approx \frac{1}{p^{1/2}} + \frac{4\delta_1}{c} [p^{1/2} - (p - c)^{1/2}] + \frac{4\delta_2}{1 - c} (p - c)^{1/2}, \quad (2)$$

where $\tau = (2z/m)^{1/2} t$, $L = L_1 + L_2$, $\delta_1 = d_1/L$, and $\delta_2 = d_2/L$. Figure 2, which plots Eq. (2) as a function of c for various $p > c$, demonstrates the presence of a high-order focus at $V_1 \approx 0.6V_2$. This point has been experimentally confirmed to high accuracy by LAMS. A small, reproducible correction for the time spent in the analytical grid region may be added to obtain elemental peak assignments that are

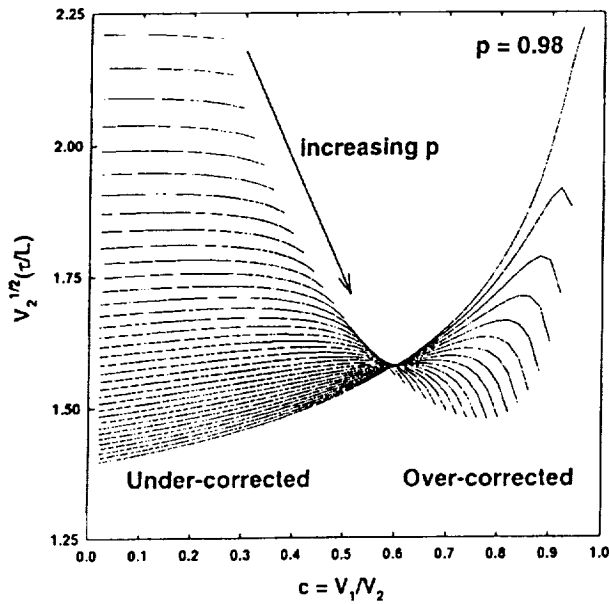


FIG. 2. Approximate one-dimensional model of the scaled TOF in LAMS as a function of $c = V_1/V_2$ for various $p = V/V_2$. Since ions with $V < V_A$ are rejected by the discrimination grids (see the text), only those with $V > V_A > V_1$, penetrating into the second reflection region, are shown.

reliable enough for autonomous operation. An example one-dimensional plot of ion trajectories (height y vs τ) is shown in Fig. 3. The ion energies in the plot range linearly from V_A to V_2 in 5 eV steps for clarity. A realistic distribution of trajectories would show a density of lines varying according to the window (V_A, V_2) on the intrinsic ion kinetic energies (often modeled as a modified Boltzmann distribution for ablation).

C. Detection and sensitivity

The microchannel plates are operated within the “current mode” range $1.6 \text{ kV} \leq |V_D| \leq 2 \text{ kV}$. The output current

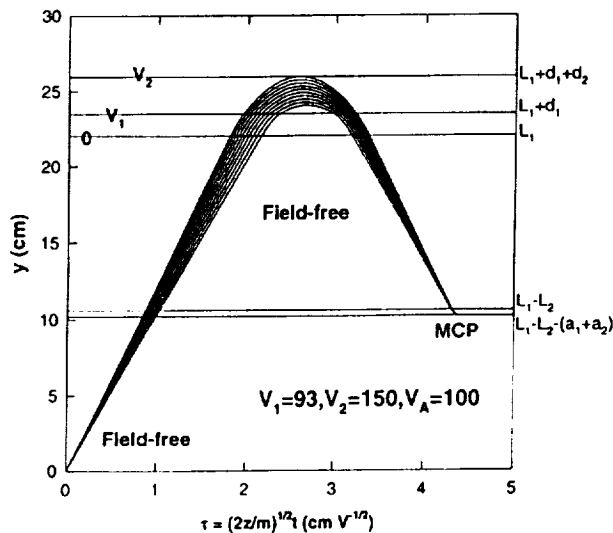


FIG. 3. One-dimensional model of the ion position as a function of scaled TOF for LAMS. Each trajectory represents an ion with a particular initial kinetic energy between V_A and V_2 . The energy step size shown in 5 eV for clarity.

as a function of time is digitized as a voltage by two channels of a Tektronix TDS 744A oscilloscope set at different gains. Signals exceeding the 8 bit range of the high-gain channel are stored as a low-gain value to give a net signal capability with a wide dynamic range. An entire spectrum is recorded in under 60 μs . Shot to shot intervals are limited by data processing and the laser duty cycle. (Currently, LAMS records spectra at 0.1–0.2 Hz.)

The average transmission and sensitivity of LAMS may be estimated by working forward from the sample volume and backward from the measured MCP signal.¹⁸ For a rocky sample material of 2 g cm^{-3} , approximately 10^{13} atoms (1 ng) are ablated from the target surface. However, an average moderate-irradiance, narrow-window current versus time LAMS spectrum on a terrestrial basalt sample integrates to $\sim 5 \times 10^{-9} \text{ C}$, or $\sim 3 \times 10^{10}$ electrons. At the gain and efficiency of the MCP, this corresponds to $\sim 10^5$ ions detected over the TOF. The eight-order difference between ablation and detection is accounted for by the ionization efficiency and the transmission. The transmission attenuation is due to three factors: (1) the acceptance angle of the MCP hole, (2) the transparency of the grids, and (3) the energy window. We estimate the MCP aperture introduces a factor of $\sim 10^{-3}$ based on the 0.05 rad opening half angle and the expected forward plume bias. Approximately one order (10^{-1}) is caused by collisions with and scattering from the grids. The energy window factor is between 10^{-2} and 10^{-1} for narrow-window spectra. Therefore, the transmission is 10^{-6} – 10^{-5} . The average ionization efficiency is then approximately 10^{-2} – 10^{-3} . (The ionization efficiencies for particular species may vary, but they are expected to approach unity as the irradiance is increased above $\sim 1 \text{ GW cm}^{-2}$.) In conventional units, the sensitivity is $\sim 5 \text{ C g}^{-1}$.

III. RESULTS AND DISCUSSION

Our assessment of the quantitative capability of LAMS has involved measurements of a range of standard and unknown target materials of scientific interest (metals, rocks, clays, etc.). From standard materials, we can determine the relative sensitivity of LAMS to specific elements within a range of energy windows, and variations between matrix types. Unknown targets, presented as blinds, provide the best tests of the ability of LAMS to distinguish major subtypes (as in petrology or meteoritics) and of the limits of inferential mineralogy (probabilistic norms). All materials can be used to study isotope ratios. We present here results for the National Institute of Standards and Technology (NIST) standard reference material (SRM) C1154a steel (19Cr–13Ni stainless), a Co–W carbide, and a terrestrial desert basalt.

A. SRM C1154a steel

The known elements in SRM C1154a, as provided by NIST, are C, N, Si, P, S, V, Cr, Mn, Fe, Ni, Co, Cu, Nb, Mo, Ta, and Pb, and all but P, S, and Pb were detected within a few laser shots. In addition, the elements H, B, O, K, Ca, Sc, Zn, and As were regularly observed in well-defined energy ranges in both surface and at-depth spectra. We analyzed the relative elemental and isotopic sensitivities with a simple

TABLE I. Comparison of NIST and LAMS measured atomic abundances for SRM C1154a in various energy windows. Asterisks denote sums excluding the isobaric m/z peaks (50), (54), and (58): $V^* = (51)$, $Cr^* = (50) + (52) + (53)$, $Fe^* = (56) + (57)$, and $Ni^* = (60) + (61) + (62) + (64)$. NIST percentages with parentheses are not certified. Table entries with "..." did not have sufficient data to be calculated.

| Element | NIST | | (35, 45) | | (45, 55) | | (55, 65) | | (65, 80) | | (80, 110) | | (110, 150) | | (150, 200) | |
|----------|---------|---------|-----------|----------|-----------|----------|-----------|----------|-----------|----------|-----------|----------|------------|----------|------------|----------|
| | (wt. %) | (at. %) | \bar{x} | σ | \bar{x} | σ | \bar{x} | σ |
| B | 0 | 0 | 0.06 | 0.03 | 0.07 | 0.05 | 0.03 | 0.02 | 0.00 | 0.00 | ... | ... | ... | ... | ... | ... |
| C | 0.100 | 0.457 | 0.07 | 0.04 | 0.26 | 0.20 | ... | ... | ... | ... | 0.05 | 0.11 | ... | ... | ... | ... |
| N | (0.077) | (0.302) | 0.03 | 0.02 | 0.04 | 0.02 | ... | ... | ... | ... | ... | ... | ... | ... | ... | ... |
| O | 0 | 0 | 0.13 | 0.07 | 0.27 | 0.34 | 0.32 | 0.46 | 0.42 | 0.86 | 0.15 | 0.29 | ... | ... | ... | ... |
| Si | 0.530 | 1.035 | 0.94 | ... | 0.63 | ... | 0.34 | 0.10 | 0.00 | 0.06 | ... | ... | ... | ... | ... | ... |
| P | 0.060 | 0.106 | 0.015 | 0.009 | ... | ... | ... | ... | ... | ... | ... | ... | ... | ... | ... | ... |
| S | 0.051 | 0.087 | ... | ... | ... | ... | ... | ... | ... | ... | ... | ... | ... | ... | ... | ... |
| Cl | 0 | 0 | 0.02 | 0.02 | ... | ... | ... | ... | ... | ... | ... | ... | ... | ... | ... | ... |
| K | 0 | 0 | 0.14 | 0.11 | 0.03 | 0.04 | ... | ... | 0.08 | 0.08 | 0.01 | 0.08 | 0.35 | 0.20 | 0.90 | 0.65 |
| Ca | 0 | 0 | 0.05 | 0.03 | ... | ... | ... | ... | ... | ... | ... | ... | 0.69 | 0.33 | 2.14 | 0.97 |
| Ti | (0.004) | (0.005) | ... | ... | ... | ... | ... | ... | ... | ... | ... | ... | ... | ... | ... | ... |
| V^* | 0.135 | 0.145 | 0.27 | 0.15 | 0.85 | 0.27 | 0.45 | 0.13 | 0.21 | 0.07 | 0.13 | 0.11 | 0.17 | 0.13 | 0.37 | 0.37 |
| Cr | 19.310 | 20.373 | ... | ... | ... | ... | ... | ... | ... | ... | ... | ... | ... | ... | ... | ... |
| Cr^* | 19.888 | 12.81 | 4.52 | 17.82 | 3.43 | 16.92 | 2.89 | 15.49 | 3.23 | 19.22 | 3.64 | 13.62 | 2.76 | 13.08 | 5.37 | ... |
| (54) | 4.146 | 4.59 | 0.31 | 4.23 | 0.72 | 4.10 | 0.40 | 4.02 | 0.34 | 4.05 | 0.43 | 4.26 | 0.42 | 4.86 | 0.69 | ... |
| Mn | 1.440 | 1.438 | 2.27 | 1.01 | 4.68 | 1.34 | 2.66 | 0.98 | 1.56 | 0.49 | 1.70 | 0.56 | 1.73 | 0.82 | 2.21 | 1.44 |
| Fe | 64.043 | 62.908 | ... | ... | ... | ... | ... | ... | ... | ... | ... | ... | ... | ... | ... | ... |
| Fe^* | 59.039 | 63.22 | 3.87 | 58.01 | 1.77 | 63.97 | 4.16 | 62.83 | 5.09 | 62.69 | 4.15 | 60.15 | 3.39 | 60.90 | 10.24 | ... |
| (58) | 8.502 | 9.63 | 1.51 | 7.64 | 1.58 | 7.74 | 1.46 | 8.25 | 1.27 | 7.99 | 0.88 | 8.86 | 1.17 | 8.99 | 1.80 | ... |
| Ni | 13.080 | 12.224 | ... | ... | ... | ... | ... | ... | ... | ... | ... | ... | ... | ... | ... | ... |
| Ni^* | 3.934 | 4.60 | 0.86 | 3.94 | 0.88 | 3.67 | 0.67 | 4.02 | 0.75 | 3.73 | 0.78 | 5.33 | 0.89 | 6.57 | 1.56 | ... |
| Co | 0.380 | 0.65 | 0.16 | 1.09 | 0.40 | 0.87 | 0.35 | 0.58 | 0.15 | 0.43 | 0.11 | 0.60 | 0.11 | 0.78 | 0.24 | ... |
| Cu | 0.440 | 0.43 | 0.08 | 0.44 | 0.12 | 0.38 | 0.14 | 0.45 | 0.15 | 0.29 | 0.23 | 0.74 | 0.21 | 1.01 | 0.56 | ... |
| As | 0 | 0.11 | 0.03 | 0.05 | 0.04 | 0.00 | 0.13 | 0.05 | 0.05 | 0.08 | 0.11 | 0.55 | 0.20 | 1.09 | 0.69 | ... |
| Nb | (0.220) | (0.130) | 0.10 | 0.26 | 0.43 | 0.31 | 0.52 | 0.94 | 2.08 | 3.41 | 0.45 | 0.25 | 1.65 | 0.74 | 2.93 | 2.39 |
| Mo | 0.068 | 0.039 | ... | ... | ... | ... | ... | ... | ... | ... | ... | ... | ... | ... | ... | ... |
| Ta | (0.045) | (0.014) | ... | ... | ... | ... | ... | ... | ... | ... | ... | ... | ... | ... | ... | ... |
| Pb | 0.017 | 0.005 | ... | ... | ... | ... | ... | ... | ... | ... | ... | ... | ... | ... | ... | ... |
| Mean TDY | | | 59.90 | | 37.04 | | 27.46 | | 29.02 | | 33.82 | | 40.47 | | 42.34 | |

protocol as follows. First, the reflectron voltages were set to a particular energy band-pass window, beginning with highest range of $(V_A, V_2) = (150, 200)$ V. The sample height was adjusted so that the surface was slightly below the laser focus (minimum beam waist diameter). With the detector voltage at a fixed $V_D = 1.8$ kV, the laser power was varied until clear, reproducible spectra were observed. This "working" laser power was set between the points where the singly and doubly ionized peaks were just visible above the background. In SRM C1154a, the dominant $^{56}Fe^+$ peak was always the first signal to appear at low power and among the first peaks to appear doubly ionized at higher power. (Recognizing spectra where $^{56}Fe^{2+}$ interfered with $^{28}Si^+$ was not a problem, as the isotopes of Fe and Cr were observed to doubly ionize as a group, producing a different peak pattern than that of the Si isotopes.) A series of 50 TOF spectra were then recorded, mass scaled, and integrated, and the procedure repeated for each of the seven windows: $(V_A, V_2) = (150, 200)$, (110, 150), (80, 110), (65, 80), (55, 65), (45, 55), and (35, 45) V. Spectra below 35 V required a significant decrease in laser energy and contained many broadened and asymmetrical peak shapes. These could not be analyzed in equal terms with the other windows and were neglected in this initial study.

Table I compares the measured LAMS signal in the seven energy windows to the values provided by NIST for

this target. In the first column, elements denoted by asterisks (V, Cr, Fe , and Ni) exclude the isobaric isotope peaks m/z (54) and (58). The values for these shared peaks are compared to $(54) = ^{54}Cr + ^{54}Fe$ and $(58) = ^{58}Fe + ^{58}Ni$ using standard terrestrial isotopic abundances. In the case of m/z (50), the small fraction (3.5×10^{-6}) due to V was neglected. The NIST weight and atomic percentages are given in the second and third columns, with uncertified values in parentheses. As the LAMS signal is a current proportional to the number of detected ions, measured values should be compared to the atomic percentage. The Table I entries are averages of raw signal integrals as ratios of the total detected ion yield (TDY). The TDY is the raw signal integral over the entire TOF range, above a fitted baseline. It may be considered an empirical proxy to the output of the complex ablation and ionization processes in LAMS. Entries denoted as "..." denote insufficient data and/or failed peak detection.

The results in Table I are from the subset of the 50 laser shots within the range $10 < TDY < 100$. Below $TDY \sim 10$, only the major peaks of Cr, Fe , and Ni were observed, and quantitative results were extremely sensitive to baseline fitting. Above $TDY \sim 100$, the major peaks tended to saturate the low-gain channel of the oscilloscope, precluding a major-to-minor element comparison and any absolute percentages. The number of spectra averaged thus ranged from 31 to 45.

As may be inferred from Table I, relative elemental sen-

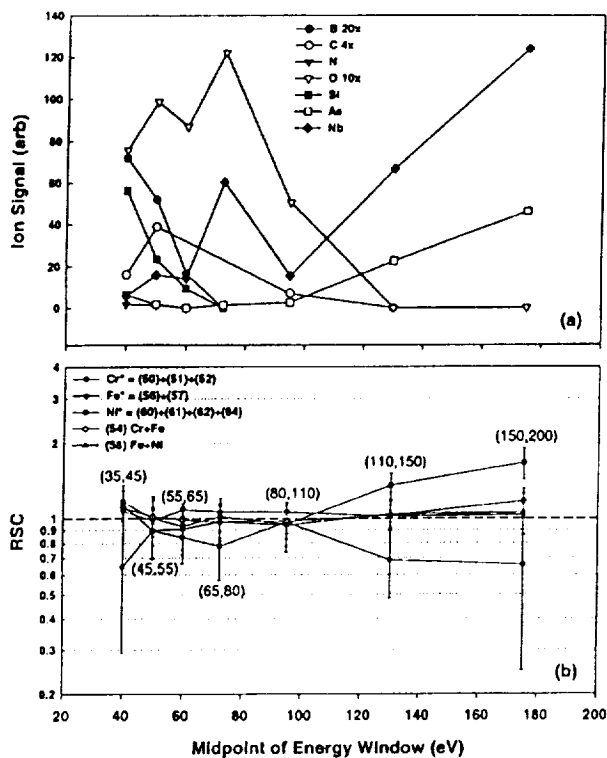


FIG. 4. LAMS results for NIST SRM C1154a steel. (a) Net ion signal vs kinetic energy window midpoint for B, C, N, O, Si, As, and Nb. The B, C, and O points are scaled for clarity. (b) RSC calculated as the ratio of measured to expected atomic abundance for Cr, Fe, and Ni. Major isobaric m/z values 54 and 58 are evaluated separately using standard terrestrial isotopic percentages. The points are positioned at energy midpoints, and the window endpoints are shown as (V_A, V_2) .

sivities and abundance precision depended strongly on the ion kinetic energy range. The lowest-mass elements (B through P) were only found in the lower-energy windows. Individual-window abundances for C, N, Si, and P fell significantly below their known bulk values. This observation is in agreement with results from another NIST steel sample,¹⁹ and with the expectation that lower-mass ions generally have lower mean kinetic energies in laser ablation.²⁰ The total LAMS signals (abundance weighted by mean TDY) for seven elements are plotted as a function of energy window midpoint in Fig. 4(a). B, C, and O data are scaled for clarity.

Interpreted as kinetic energy spectra, the signals for C and O correspond to distributions with means of ≤ 50 –70 and ~ 50 –80 eV, respectively. These means are upper bounds, as they assume that the behavior below (35, 45) eV is a simple extension of the observed trends. In fact, there is preliminary evidence²¹ for a large increase in carbon ions below 30 eV in NIST steels. The total carbon integral is thus expected to be closer to the expected value than the limited energy range data presented here. Similarly, the signals for B and Si increase for lower energies, implying spectra with means below (35, 45) eV.

Heavier elements (K through Nb) were detected across the entire energy range measured. The highest-mass elements observed reproducibly (As and Nb) were increasingly prevalent with increasing energy, as expected [Fig. 4(a)]. In the (35, 45) eV band, ⁹³Nb was emitted with an approximately accurate atomic abundance, but it increased to more than 20 times the expected value at the highest energies, in agreement with the behavior of the neighboring element Mo in another NIST steel.^{19,22} This increase may be due to more than individual window fractionation alone. Within the energy range scanned, the “total” relative resistivity coefficients (RSCs) (from the signal summed over all the windows) for the heavy elements were also anomalously high.

The major transition metal elements V through Cu were directly accurate to within 5%–20% in several energy windows. The ratios of measured to expected atomic percentage, or RSCs, for the major elements Cr, Fe, and Ni are plotted as a function of the energy window midpoint in Fig. 4(b). The error bars correspond to one standard deviation. The observed RSC values for these elements suggest flatter energy spectra than those seen for the minor elements. Of particular note is the enhanced accuracy and precision for these elements in the band (80, 110) eV. The best average accuracy for the minor transition metals V, Mn, Co, and Cu (not plotted) also coincided with this window, where all four elements exhibited broad minima in their TDY-weighted signals. This energy spectrum minimum, which follows from the mean TDY variation (Table I), may be an intrinsic feature of laser-ablated metals, exhibiting “thermal” (~ 10 eV) and “accelerated” (~ 100 eV) energy peaks.^{9,23}

In Table II, the measured minor isotopic abundances are compared to standard terrestrial values. Ratios were taken

TABLE II. Comparison of standard and measured minor isotopic abundances in SRM C1154a for various energy windows.

| Elements | Std % | (35, 45) | | (45, 55) | | (55, 65) | | (65, 80) | | (80, 110) | | (110, 150) | | (150, 200) | |
|-------------------|-------|-----------|----------|-----------|----------|-----------|----------|-----------|----------|-----------|----------|------------|----------|------------|----------|
| | | \bar{x} | σ | \bar{x} | σ | \bar{x} | σ |
| ¹⁰ B | 18.98 | 20.19 | 4.91 | 21.38 | 6.43 | ... | ... | ... | ... | ... | ... | ... | ... | ... | ... |
| ¹³ C | 1.11 | 1.28 | 0.76 | 1.14 | 0.06 | 1.20 | 0.18 | 1.28 | ... | ... | ... | ... | ... | ... | ... |
| ²⁹ Si | 4.71 | 5.53 | 0.04 | 5.73 | 0.30 | 5.55 | 0.18 | ... | ... | ... | ... | ... | ... | ... | ... |
| ³⁰ Si | 3.12 | 2.97 | 0.42 | 3.86 | 1.12 | 2.72 | 0.17 | ... | ... | ... | ... | ... | ... | ... | ... |
| ³⁷ Cl | 24.23 | 24.48 | 1.85 | ... | ... | ... | ... | 24.99 | 0.40 | ... | ... | ... | ... | ... | ... |
| ⁵⁰ Cr* | 4.40 | 4.11 | 0.38 | 3.73 | 0.34 | 3.72 | 0.38 | 3.78 | 0.39 | 3.28 | 0.40 | 4.39 | 1.18 | 6.73 | 1.97 |
| ⁵³ Cr* | 9.78 | 10.01 | 2.10 | 13.67 | 3.79 | 11.00 | 2.79 | 9.75 | 2.83 | 8.69 | 1.48 | 9.90 | 2.30 | 12.90 | 2.67 |
| ⁵⁷ Fe* | 2.33 | 4.02 | 0.89 | 7.74 | 1.68 | 3.92 | 0.99 | 3.06 | 0.86 | 2.67 | 1.01 | 3.03 | 0.58 | 4.05 | 1.16 |
| ⁶¹ Ni* | 3.70 | 6.37 | 1.28 | 8.67 | 1.79 | 8.72 | 2.32 | 5.15 | 1.04 | 4.45 | 1.72 | 5.54 | 1.82 | 6.30 | 2.05 |
| ⁶² Ni* | 11.38 | 12.31 | 1.71 | 11.58 | 1.86 | 12.66 | 2.20 | 12.73 | 2.06 | 11.50 | 0.90 | 13.24 | 1.94 | 15.63 | 2.60 |
| ⁶⁴ Ni* | 3.36 | 4.31 | 0.59 | 4.09 | 1.04 | 4.08 | 1.17 | 3.90 | 1.21 | 2.84 | 0.65 | 4.82 | 2.04 | 5.46 | 2.78 |
| ⁶⁵ Cu | 30.91 | 32.23 | 6.97 | 30.32 | 6.22 | 31.26 | 9.41 | 30.95 | 6.90 | 29.34 | 4.88 | 31.07 | 3.08 | 29.72 | 2.36 |

with respect to the total elemental detected yield (EDY), or for elements with isobaric interferences, the unambiguous subtotal (as introduced above). Performance without any standardization or elemental envelope adjustment was very good. Ratios for ^{10}B , ^{13}C , ^{37}Cl , ^{50}Cr , ^{62}Ni , and ^{65}Cu had an uncorrected average accuracy of less than 7%. Energy-dependent isotopic fractionation is not expected to be as significant as it is for elements, but some marked anomalies did occur in the (45, 55) and (150, 200) eV range. It was discovered that, in these cases, the number of spectra in which isotope measurements could be reliably made was reduced. Increasing counting statistics for averaging will probably smooth the observed sensitivity trends. Isotopic abundance accuracy for these elements increased with separation from the dominant ^{56}Fe peak, implying that baseline and peak shape sensitivity introduced systematic errors. A striking example of this effect is the $^{65}\text{Cu}/\text{Cu}$ value, with an average standard deviation of 2.4%. The total Cu content of C1154a is only 0.38 at. %, but the absence of any broadened neighboring peaks permitted a highly reproducible measurement. Isotopic accuracy for the minor elements also increased with EDY, as expected, given the constancy of the baseline noise. For those spectra in the top 10% of the EDY range for a given minor element, sub-1% errors were regularly observed (although insufficient data were obtained in this range to calculate σ).

The single-shot detection limit in SRM C1154a was estimated as 18 ppm atom by the detection of ^{34}S with a signal-to-noise ratio of 2. Due to the high reproducibility of the peak positions, automated averaging of spectra should provide improvements approaching the $N^{-1/2}$ dependence with random noise. The average resolution for most peaks in the low-mass range was $m/\Delta m \sim 200$ using the half-width at half-maximum definition.

The overall performance with this standard steel was quite encouraging, given the modest number of spectra averaged and the ability of the small laser spot to sample the heterogeneity of the target. The elemental and isotopic accuracy equals or exceeds that of other laser mass spectrometric methods when no standards are used.¹¹ The middle energy range of high reproducibility indicates that a LAMS calibration can be obtained for accurate measurement of "neighboring" elements within a single energy window, reducing the overall energy scanning. The narrow-window view works well here for absolute abundances because this neighboring element sequence comprises the vast majority of atoms in the solid. More generally, such a calibration would be most suitable for nearby-element ratios (e.g. to Fe), which are not sensitive to absolute fluctuations of the considered mass range.

To better understand the fractionation behavior of low-energy ions in LAMS, we performed a separate analysis of a Co-W carbide target. Due to the simpler stoichiometry of the carbide relative to C1154a, we were able to obtain reproducible elemental yields to below 10 eV, with 5 eV windows. A sensitivity much closer to the total RSC could thus be obtained by integrating the entire energy range. A simple scan was recorded from a fresh surface for each of two incident laser irradiances, $I_1 = 0.77 \text{ GW cm}^{-2}$ and I_2

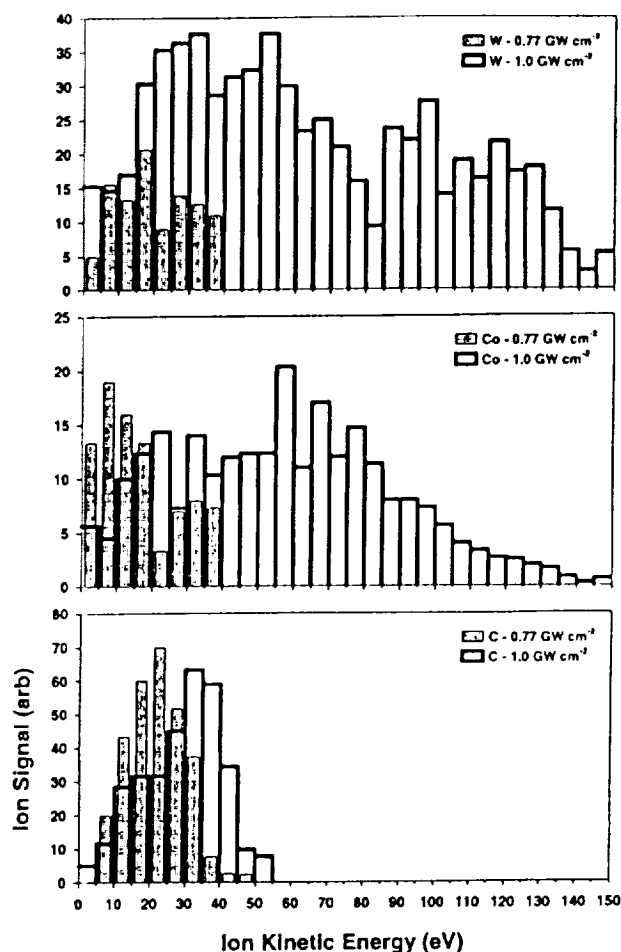


FIG. 5. Ion kinetic energy spectra for C, Co, and W in a carbide LAMS target. The energy range was scanned in 5 eV steps for each of the two laser irradiances ($I_1 = 0.77 \text{ GW cm}^{-2}$ and $I_2 = 1.0 \text{ GW cm}^{-2}$).

$= 1.0 \text{ GW cm}^{-2}$. Figure 5 shows the raw distributions obtained for the three elements C, Co, and W. These elements are well separated in the TOF spectra (mean $m/z = 12$, 59, and 184 amu/e), and their low-energy spectra were unambiguously integrated. The plots demonstrate the sensitivity of ionization to the species and the laser power density. As expected from the NIST steel studies, C was found almost entirely below 50 eV. The total carbon signal increased by only a factor of 1.11 from I_1 to I_2 (from 295 to 327), while the Co and W signals increased manyfold (2.86 and 7.29 times, respectively). When compared to the certified atomic abundance ratios (C/Co 1.36, C/W 1.29), there was a large relative excess of C (C/Co 3.38, C/W 2.91) at low irradiance, but W/Co was accurate to within 10%. At high irradiance, there was a relative excess of W, but C/Co agreed to within 3% (C/Co 1.31, C/W 0.44).

The irradiances used here are near the lower end of the "hot plasma" range,⁹ in which the ionization efficiency is fairly uniform and near 100%, and the ablation mass is proportional to $I^{1/2}/m^{1/4}$. For a given laser shot in this range, higher-mass atoms are ablated less efficiently (although weakly so). However, Co and W also have lower ionization potentials than C. At irradiances below $\sim 1 \text{ GW cm}^{-2}$, the fractions of ablated Co and W atoms that are ionized will be

enhanced, countering the ablation mass trend. (Above $\sim 1 \text{ GW cm}^{-2}$, the dependence on the ionization potential dissipates.)²⁴ Thus the irradiance regime used may host competing fractionation trends, with total RSCs that are quite sensitive to fluctuations in laser coupling and sample heterogeneity. The increases in Co/C and W/C with I may indicate that the "hot" range is attained for Co and W at lower irradiance than for C. This trend is consistent with the anomalously high total RSCs for higher-mass elements seen in other targets. The high-irradiance W ion energies also exhibited a double-peaked distribution, with means of $\sim 40\text{--}50$ and $\sim 110\text{--}120 \text{ eV}$. The complexity introduced by the sensitivity to irradiance and by possible multimodal energy spectra²⁵ indicates that any autonomous operation of LAMS should include a general scan of a wide energy range, in addition to sequences of shots within select narrow windows as described above.

B. Terrestrial basalt

As a more realistic target for future *in situ* studies, we have begun to examine a terrestrial desert basalt sample with LAMS. The specimen was presented as a "partial" blind (the exact origin and mineralogy have not been disclosed), and the subclassification analysis is ongoing. Preliminary studies of the basalt have already been quite helpful in assessing the reproducibility of elemental and isotopic yields, as well as the ability of LAMS to probe into the subsurface layers of rocky materials.

Detected elements were H, C, O, Na, Mg, Al, Si, P, K, Ca, Ti, V, Mn, Fe, and a few rare earths at trace levels. Spectra were clearly distinguishable between surface and bulk types and between "high Fe" and "low Fe" within the bulk. Sequences recorded at a fixed location, but at varying depths, changed between high-Fe and low-Fe types within a few shots, similar to the behavior seen in a carbonaceous chondrite target.¹⁹ Figure 6(a) shows an example single-shot bulk spectrum from the basalt target in the energy window (65, 75) eV. It is typical of the high-Fe bulk regions (atomic Fe/Si > 3, vs the ~ 0.2 expected) observed in approximately 1/3 of the spectra in this range. The low-Fe spectra comprising the remaining bulk measurements were clustered around Fe/Si ~ 1 . Averaged abundance ratios therefore reflect the strong fractionation bias (in this narrow energy range) toward higher masses as seen in other targets. Similarly, the spectra were markedly low in O (atomic O/Si < 0.5 versus the ~ 3 expected).

Isotopic ratios were more accurate and reproducible in this target than in any of the metal alloys examined. The minor isotope abundances in the Mg-Ti series agreed to within 5%, the maximum observed standard deviation of raw signal ratios. Figure 6(b) shows Ti isotope data for 22 laser shots. The increase in relative sensitivity from -5% to $+5\%$ may reflect an intrinsic bias toward higher masses, as was seen in SRM C1154a, but over a much narrower mass range. This trend was slightly modulated according to the baseline fitting method, but the overall errors were stable. Highly reproducible and accurate isotope ratios in this mass range were also observed in a carbonaceous chondrite meteorite.¹⁹

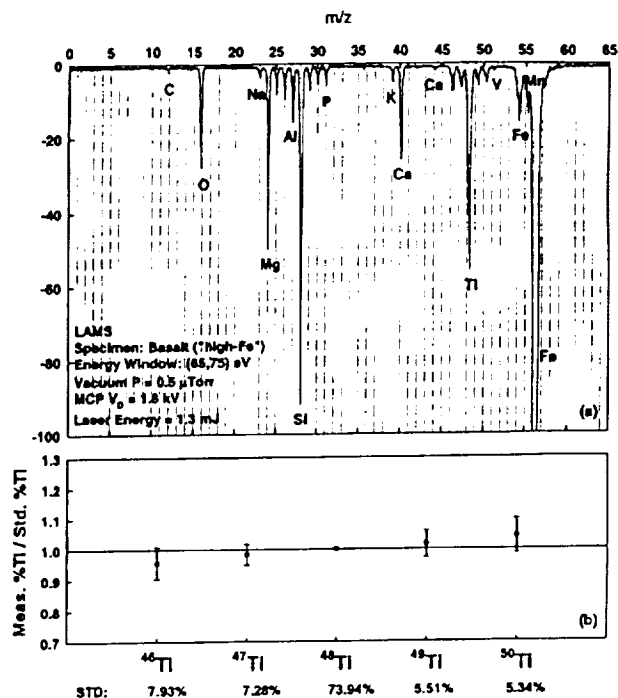


FIG. 6. Terrestrial desert basalt results from LAMS. (a) Sample single-shot spectrum from a "dark" bulk region in the energy window (65, 75) eV. (b) Measured isotopic abundances for Ti compared to expected terrestrial values in basalt. Standard percentages are shown below the isotope masses. The error bars correspond to one standard deviation for 22 laser shots.

The potential to distinguish mineralogical regions with LAMS has led to a focus on surface layer analyses. Surface layers on rocky materials are known to arise from various processes reflective of the interaction of the material with its environment over time. By microscopically studying a rock from its surface inward, we may infer the history of aqueous, wind-borne, biogenic, and other processes in the vicinity of the exposed surface. This analysis is of particular importance for *in situ* probes, which must access material within and below a weathered surface, to properly determine the rock type and geological context. The basalt target (observed through the LAMS imager) had a mottled surface indicative of weathering. We examined a sequence of 150 spectra in a (140, 150) eV window from a fresh surface to see if a rock varnish²⁶ could be detected from LAMS spectra. The raw atomic Mn/Fe, (Na+K)/Si, and Al/Si ratios were monitored in real time and plotted (Fig. 7).

Nearly every spectrum contained Mn and Fe, while approximately 20 out of the 150 shots did not generate sufficient signal to measure the Na+K and Al ratios, giving those plots a more decimated appearance. The Mn/Fe ratio began at a high, constant value (>1), then dropped precipitously after ~ 70 shots to a value more in line with terrestrial basalts. With the estimated $0.2\text{--}0.3 \mu\text{m}$ per shot, the detected layer was $\sim 15\text{--}20 \mu\text{m}$ thick. This is the expected behavior for varnish layers, which are known to be high in Mn due to the presence of a manganese oxide known as bimesite.²⁶ Due to the usual inclusion of Na and K atoms in this mineral, the atomic ratio of (Na+K)/Si was also of interest. From the plot, it clearly had similar behavior to Mn/Fe. Since the Si

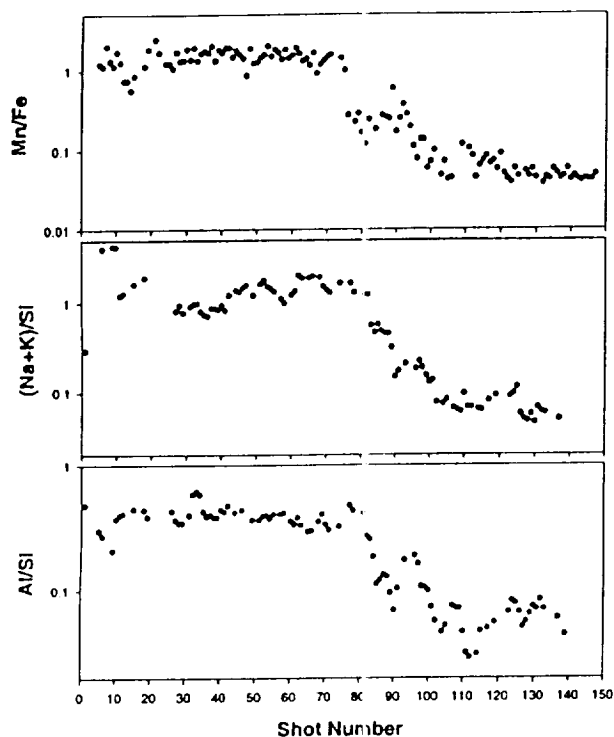


FIG. 7. Monitored total element atomic ratios in basalt as a function of laser shot number from an unanalyzed weathered surface. The vertical scale is logarithmic. The ablated (crater) depth is approximately $0.2\text{--}0.3\ \mu\text{m}$ per shot.

abundance was constant, within experimental precision, over the entire sequence, the transition is between regions of high and low Na+K. The “bulk” value of $(\text{Na}+\text{K})/\text{Si} \sim 0.07$ is lower than, but comparable to, the expected range for basalts ($\sim 0.11\text{--}0.13$).²⁷ The third ratio monitored, Al/Si , shows the same qualitative behavior, with a highly reproducible varnish layer value of ~ 0.4 , but with a less pronounced drop into the bulk phase than the other two ratios. We are not aware of a high aluminum oxide characteristic of rock varnish, and this is the only other element ratio that showed a significant layer transition. (Conspicuously absent was a variation in C. High C from magnetotactic bacteria discussed in some theories of rock varnish would be expected to drop in the bulk phase. However, almost no C was detected in the high energy window used here.)

C. Instrument outlook

The results for LAMS thus far are very encouraging for high sensitivity and quantitatively based *in situ* classification of major rock and soil types. The highly miniaturized design of LAMS also permits its use in a multicontext mission, where several samples are taken from a wide area. The depth ability with the basalt demonstrates LAMS access to bulk, unweathered material. The degree of accuracy and precision in science return from a mission including LAMS will depend both on the overall instrument suite (the complementarity of multiple detectors), and on *a priori* knowledge of the intrinsic relative sensitivities in LAMS. The initial calibration of RSCs on standard and unknown targets has been described in this article. A much wider range of experimental

conditions and materials is currently under investigation, and should lead to a “flight-ready” approach for unknown *in situ* samples.

Determining the empirical relationship between the LAMS detector output and the elemental and isotopic abundances within the analyte is the goal for assessing quantitative ability. The relative sensitivity coefficient is, in general, a function of the laser-target coupling, the target composition, and the LAMS ion optics and detection parameters. A good RSC calibration clearly depends on understanding the reproducibility of experimental conditions.²⁸ The ion optics and detection setup generate a fractionation that is expected to be small and reproducible for any material. Further, for bulk averages, the use of laser irradiances slightly above $\sim 1\ \text{GW cm}^{-2}$ gives high, uniform ablation and ionization efficiencies across many target types. However, the variation in laser-target coupling may lead to irreproducible experimental conditions in some cases. In particular, surface morphology fluctuations can change characteristics of the plume from shot to shot, and thus ablation is often viewed as unpredictable. For appropriately defined averages, though, reproducibility may be restored and an “intrinsic” instrumental RSC may be observed. For instance, abundances within small grains may be obtained by averaging enough spectra to detect all variations from the bulk, but few enough to remain within the grain. As such, the specific requirements for quantitative analysis with LAMS may depend on the composition information desired.

All analyses use a common energy windowing and focusing method based on the instrument description above. Normally, several windows (V_1 , V_2) are used to sample the kinetic energy distribution of emitted ionized species. The peak energies and widths of these distributions generally increase with mass, laser irradiance, and degree of ionization. For a fairly constant irradiance and single-stage ionization, spectra can be recorded and single mass peaks integrated assuming a fixed energy distribution.

Important low-mass ions such as C^+ , N^+ , and O^+ are concentrated at kinetic energies below 50 eV. It is expected that special window modes, such as calibrated combinations of narrow- and wide-window spectra, will be required to achieve the precision and sensitivity needed to address *in situ* science goals. In the laboratory prototype of LAMS, these elements may be present in the residual vacuum chamber gas. The redeposition of these elements following a laser shot can increase their effective detection limit. We are currently investigating this process with a variable-delay double-pulse laser that first removes surface contaminants and then analyzes bulk material before significant redeposition can occur.²⁹ Such “pre-cleaning” may allow closer simulation of the conditions of *in situ* analyses.

In addition to understanding the behavior of the current LAMS instrument with a range of target materials, efforts are underway to improve the sensitivity and resolution of LAMS itself. Incorporating an Einzel lens (or other ion lens) will increase the throughput via collimation. In LAMS the position and voltage range of lenses must be carefully adjusted to avoid complications due to the plasma plume. Similarly, a pulsed ion gate will permit the selective suppression of cer-

tain TOF regions to minimize any ion interaction difficulties and increase sensitivity. It too must be reexamined for miniature instrument use. The size limitations in planetary exploration also restrict the flexibility in reflectron design. Tests are currently underway with ideal, or nearly ideal, reflectron designs that correct the TOF over a much wider energy range than the two-stage LAMS unit. High-order correction in LAMS demands that component positions and electrostatic parameters be highly precise and robust.

Finally, we are testing LAMS with an ultraviolet (UV) Nd:YAG tripled (355 nm) or quadrupled (266 nm) laser that may increase its sensitivity to various species, including molecular compounds. Shorter wavelengths may also produce a smaller and more reproducible crater. However, any improvement with UV must be weighed against the increased complexity and fragility that may be required in a flight unit. The infrared (IR) laser was originally chosen to test the simplest LAMS that can provide useful results on future missions. We plan to provide a quantitative comparison of UV ablation (as found in some commercial instruments) and UV desorption (such as in MALDI-type systems) in LAMS with the IR results in a future report.

ACKNOWLEDGMENTS

The authors wish to acknowledge the advice and assistance of Dr. R. E. Gold, Dr. E. H. Darlington, Dr. E. P. Keath, Dr. S. L. Murchie, Mr. D. A. Lohr, Dr. D. E. Brownlee, and Dr. D. S. Burnett. One of the authors (G.G.M.) wishes to thank A. E. Chumikov, N. G. Managadze, and V. Leonov, and Advanced Power Technologies, Inc. (APTI), which is developing a commercial version of the LASMA device. This work was supported by NASA Planetary Instrumentation Definition and Development Program (PIDDP) Grant No. NAG5-4548, and by APL Independent Research and Development funding.

- ¹H. B. Niemann, J. R. Booth, J. E. Cooley, R. E. Harle, W. T. Kasprzak, N. W. Spencer, S. H. Way, D. M. Hunter, and G. R. Carignan, *IEEE Trans. Geosci. Remote Sens. GE-18*, 60 (1980); R. W. McEntire and D. G. Mitchell, in *Solar System Plasma Physics*, edited by J. H. Waite, J. L. Burch, and R. L. Moore, Geophysical Monograph Series (The American Geophysical Union, Washington, DC, 1989), Vol. 54; W. Kasprzak, H. Niemann, D. Harpold, J. Richards, H. Manning, E. Patrick, and P. Mahaffy, *Proc. SPIE 2803*, 129 (1996); P. R. Mahaffy, in *Laboratory Astrophysics and Space Research*, edited by P. Ehrenfreund *et al.* (Kluwer, Dordrecht, 1998), p. 355; S. Scherer, K. Altwegg, H. Balsiger, M. Hohl, H. Kastle, M. Mildner, and P. Wurz, *Proceedings of the 46th ASMS Conference on Mass Spectrometry and Allied Topics*, Orlando, FL, 1998, p. 1238.
- ²H. B. Niemann, D. N. Harpold, S. K. Atreya, G. R. Carignan, D. M. Hunten, and T. C. Owen, *Space Sci. Rev.* 60, 111 (1992); H. B. Niemann, in *Gas Chromatograph Mass Spectrometer for the Huygens Probe* [European Space Agency (ESA)-SP-1177, 1997], p. 85; V. Navale, D. Harpold, and A. Vertes, *Anal. Chem.* 70, 689 (1998).
- ³R. D. Rushneck, *et al.*, *Rev. Sci. Instrum.* 49, 817 (1978); *Planetary Science Instruments Workshop*, edited by C. Meyer, A. H. Treimann, and T. Kostiuik, LPI Technical Report No. 95-05, Lunar and Planetary Institute, Houston, 1996.
- ⁴R. J. Cotter, *Time of Flight Mass Spectrometry: Instrumentation and Applications in Biological Research* (American Chemical Society, Washington, DC, 1997).
- ⁵*Laser Ionization Mass Analysis*, edited by A. Vertes, R. Gijbels, and F. Adams (Wiley, New York, 1993).
- ⁶R. Z. Sagdeev, G. G. Managadze, I. Yu. Shutyaev, K. Szego, and P. P. Timofeev, *Adv. Space Res.* 5, 111 (1985); R. Z. Sagdeev *et al.*, *Proceedings of the International Workshop on Phobos*, Space Research Institute (IKI), USSR Academy of Sciences, Moscow, 1986, p. 7.
- ⁷The attenuator (a Spindler and Hoyer neutral wedge) consisted of a neutral density glass wedge bonded to a clear compensating plate. The transmission could be varied between 1% and 80% with a precision translation stage, although we typically operated at the high-transmission end, where the attenuation drop across the beam diameter was negligible. To obtain highly attenuated pulses, we used additional flat neutral density filters in the beam path.
- ⁸In contrast to ablation, lower laser irradiances ($I < 10^8$ W cm⁻²) sample target material by an assortment of thermal and nonthermal processes termed laser desorption. In the desorption regime, molecules and molecular fragments survive volatilization and ionization, producing spectra containing both atomic and molecular information. Depending upon irradiance and target matrix effects, identification of large molecular species including organic/biological structures is possible with desorption. The natural extension of LAMS to this lower-energy range is currently under investigation.
- ⁹C. R. Phipps and R. W. Dreyfus, in Ref. 5, Chap. 4A.
- ¹⁰L. Moenke-Blankenburg, in Ref. 5, Chap. 4B.
- ¹¹H.-J. Dietze and J. S. Becker, in Ref. 5, Chap. 4C.
- ¹²L. Moenke-Blankenburg, in *Lasers in Analytical Atomic Spectroscopy*, edited by J. Sneddon, T. L. Thiem, and Y.-I. Lee (VCH, New York, 1997), Chap. 4.
- ¹³K. Tanaka, Y. Ido, S. Akita, Y. Yoshida, and T. Yoshida, *Rapid Commun. Mass Spectrom.* 2, 151 (1988); M. Karas and F. Hillenkamp, *Anal. Chem.* 60, 2299 (1988).
- ¹⁴G. G. Managadze and I. Yu. Shutyaev, in Ref. 5, Chap. 5.
- ¹⁵R. Z. Sagdeev *et al.*, *Astron. Astrophys.* 187, 179 (1987).
- ¹⁶I. D. Kovalev, N. V. Larin, A. I. Suchkov, A. M. Voronov, and P. A. Shmonin, *Prib. Tekh. Eksp.* 6, 139 (1985).
- ¹⁷Unit mass resolution is sufficient to resolve the isotopes of any given element from each other, but is not sufficient to resolve *isobars*, i.e., the isotopes of different elements sharing the same mass number. Isobaric interferences may also arise if molecular species coincide with atomic ions, e.g., ¹⁸O and H₂O. To separate such contributions, resolutions of 10³–10⁴ are often required. For laser TOF-mass spectrometers, it may be more realistic to focus on elemental and isotopic enrichment techniques for *in situ* isobaric resolution. Examples of such techniques include chemical separation, negative-ion generation, and resonance ionization.
- ¹⁸O. J. Orient, A. Chutjian, and V. Garkanian, *Rev. Sci. Instrum.* 68, 1393 (1997).
- ¹⁹W. B. Brinckerhoff, A. F. Cheng, R. W. McEntire, and G. G. Managadze, in *Lunar and Planetary Science XXIX*, Abstract No. 1789 (Lunar and Planetary Institute, Houston, 1998).
- ²⁰J. T. Cheung and H. Sankur, *Crit. Rev. Solid State Mater. Sci.* 15, 63 (1988).
- ²¹Unpublished results.
- ²²W. B. Brinckerhoff, R. W. McEntire, A. F. Cheng, and G. G. Managadze, *Third IAA Conference on Low-Cost Planetary Missions* (International Academy of Astronautics, Pasadena, CA, 1998).
- ²³Yu. A. Bykovskii, G. I. Schuralev, V. I. Belousov, V. M. Gladskoi, V. G. Degtjarev, Yu. N. Kolosov, and V. N. Nevolin, *Fiz. Plazmy* 4, 323 (1978).
- ²⁴A. Vertes, P. Juhasz, M. De Wolf, and R. Gijbels, *Int. J. Mass Spectrom. Ion Processes* 94, 63 (1989).
- ²⁵Q. Zhuang, K. Ishigoh, K. Tanaka, K. Kawano, and R. Nakata, *Jpn. J. Appl. Phys., Part 2* 34, L248 (1995); K. Fukushima, Y. Kanka, and T. Morishita, *J. Appl. Phys.* 74, 6948 (1993).
- ²⁶See, for example, R. I. Dorn, *Am. Sci.* 79, 542 (1991).
- ²⁷P. C. Hess, *Origins of Igneous Rocks* (Harvard University Press, Cambridge, 1989).
- ²⁸F. E. Lichte, *Anal. Chem.* 67, 2479 (1995).
- ²⁹I. D. Kovalev, K. N. Malishev, and P. A. Shmonin, *J. Anal. Chem. USSR* 53, 3842 (1998).